UNIVERSITY OF CALIFORNIA,
IRVINE

Using Angular Power Spectra to Probe CIB Anisotropies

DISSERTATION

submitted in partial satisfaction of the requirements
for the degree of

DOCTOR OF PHILOSOPHY

in Physics

by

Cameron Michael Franklin Thacker

Dissertation Committee:
Professor Asantha Cooray, Chair
Professor Michael Cooper
Professor Kevork Abazajian

2014

DEDICATION

To my family for all of the support and encouragement.

TABLE OF CONTENTS

LIST OF FIGURES

LIST OF TABLES

ACKNOWLEDGMENTS

I would like to first thank my advisor, Professor Asantha Cooray, for giving me an opportunity right when I needed one the most. The timeline looks something like this: I emailed Asantha notifying him that I was dropping his Cosmology course because my current advisor had no funding for me, and I was most likely changing fields. He replies by saying I should speak to his graduate student, Joseph, and that he has both funding and research ideas. Two days later, I was in his group and already starting on research. That is the kind of person Asantha is, and one I am thankful to have had as an advisor.

Secondly, I would like to thank Dr. Joseph Smidt to whom I owe much – not only for getting me up to speed on research, but for helping to develop me into a better scientist. I am also grateful for my wonderful collegaues who provided me with endless inspiration, help, and amusement: Jon O'Bryan, Jae Calanog, Ketron Mitchell-Wynne, Ryan Keeley, Julie Wardlow, Hai Fu, Yan Gong, Francesco de Bernardis, Nicholas Timmons, and Carrollann Simmons.

Lastly, I would like the thank my friends and family for all of the love and support you have given me, both emotionally and financially (thanks, Mom). I especially want to the thank my wife, Sarah, who makes every day better – I can't imagine grad school without you!

The text of this thesis is a reprint of the material as it appears in "H-ATLAS: The Cosmic Abundance of Dust from the Far-infrared Background Power Spectrum" (ApJ 768, 58) and "Cross-Correlation of Near and Far-Infrared Background Anisotropies as Traced by *Spitzer* and *Herschel*" (ApJ submitted).

Financial support for this work was from NSF CAREER AST-0645427, NASA NNX10AD42G, NSF AST-1313319, and the GAANN fellowship.

CURRICULUM VITAE

Cameron Michael Franklin Thacker

EDUCATION

Doctor of Philosophy in Physics — **2014**
University of California, Irvine — *Irvine, CA*

Bachelor of Science in Physics & Mathematics — **2010**
University of Florida — *Gainesville, FL*

RESEARCH EXPERIENCE

Graduate Research Assistant — **2012–2014**
University of California, Irvine — *Irvine, CA*

Research Assistant — **2008–2010**
University of Florida — *Gainesville, FL*

TEACHING EXPERIENCE

Teaching Assistant — **2010–2012**
University of California, Irvine — *Irvine, CA*

REFEREED JOURNAL PUBLICATIONS

Cross-Correlation of Near and Far-Infrared Background Anisotropies as Traced by *Spitzer* and *Herschel* — **2014**
ApJ, Submitted

H-ATLAS: The Cosmic Abundance of Dust from the Far-infrared Background Power Spectrum — **2013**
ApJ

POSTER PRESENTATION

H-ATLAS: The Cosmic Abundance of Dust from the Far-infrared Background Power Spectrum — **January 2013**
221st AAS Conference

Theoretical Insights on Surface Absorbtion and Electronic Spectra of CdSe Quantum Dots Functionalized by Ru-bipyridine Complex **August 2009**
Excited State Processes in Electronic and Bio Nanomaterials

HONORS & AWARDS

NASA Group Achievement Award **2014**
University of California, Irvine

GAANN grant recipient **2012-2014**
University of California, Irvine

Regents Fellowship **20102011**
University of California, Irvine

Outstanding Poster **2009**
Excited State Processes in Electronic and Bio Nanomaterials, Santa Fe, NM

Center for Condensed Matter Sciences Undergraduate Fellowship **2009**
University of Florida

ABSTRACT OF THE DISSERTATION

Using Angular Power Spectra to Probe CIB Anisotropies

By

Cameron Michael Franklin Thacker

Doctor of Philosophy in Physics

University of California, Irvine, 2014

Professor Asantha Cooray, Chair

I present my work involving the auto and cross-power spectra of the cosmic infrared background (CIB) anisotropies. Specifically, I use data that comes from both ends of the infrared spectrum. In this thesis I measure the angular power spectrum in the far-infrared with data from the *Herschel Space Observatory* at 250, 350, and 500 μm wavelengths and interpret this through a halo model using a conditional luminosity function approach. Integrating over the dusty galaxy population responsible for the background anisotropies, I then calculate the cosmic density of dust. Finally, I measure, for the first time, the cross-correlation of near and far-infrared background anisotropies using the *Spitzer Space Telescope* at 3.6 μm and *Herschel*. The cross-correlation is modeled using a halo model with three components: (a) far-IR dusty galaxies in *Herschel*, (b) near-IR faint galaxies below the masking depth at 3.6 μm, and (c) intra-halo light, or diffuse stars in dark matter halos, likely dominating fluctuations at 3.5 μm.

Chapter 1

Introduction

The cosmic infrared background (CIB) is similar to the cosmic microwave background but is from the epoch of reionization (EoR) until now (Fig. 1.1). Studying the epoch of reionization is the holy grail of CIB studies. However, the problem is that the CIB contains the total emission history of the Universe integrated along the line of sight. Within this signal are the redshifted emssions from the first stars, but the dominant contributions are from lower redshift sources.

Due to Earth's atmosphere being opaque in much of the infrared, it wasn't until 1990 that technology and funding was in place and the Cosmic Background Explorer (COBE) Diffuse Infrared Background Experiment (DIRBE) instrument was able to make the first reliable limits on the CIB at ten bands ranging from 1.25 to 240 μm and thus began the observational CIB era. Since then, there have been numerous infrared instruments including, WMAP, *Planck*, *Hubble*, *Spitzer*, *Herschel*, and others.

In the first chapter we make use of one of the extragalactic fields of the *Herschel* Astrophysical Terahertz Large Area Survey (H-ATLAS) at 250, 350, and 500 μm far-IR bands. While the total intesnsity of the cosmic far-IR background (CFIRB) is known from absolute photometry

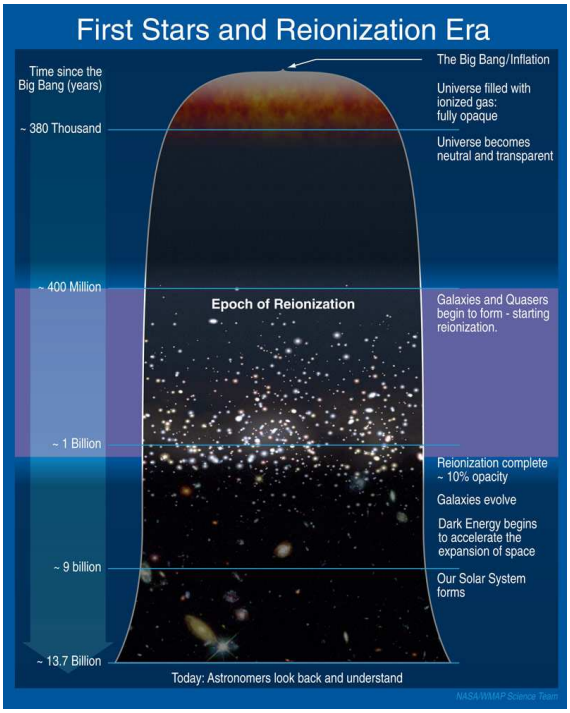

Figure 1.1: NASA graphic highlighting the epoch of reionization in the cosmic timeline.

(Puget et al., 1996; Fixen et al., 1998; Dwek et al., 1998), we still lack a complete knowledge of the sources, in the form of dusty star-forming galaxies that make up the background. For example, at 250, 350, and 500 μm, only 5, 15, and 22% of the total background intensity is resolved into individual galaxies (Oliver et al. , 2010). To get around this limitation, we instead use the anisotropies, or spatial fluctuations of the background.

These spatial fluctuations in the CIB are best studied using the angular power spectrum. This technique was borrowed from CMB analysis and modified from a full sky measurement to one using the flat sky approximation (See Appendix A.2). The Appendix section A.3 shows how we calculate the anisotropy power spectrum. Using this, we have a method to extract information about large scale structure. Even though galaxies may not be individually detected, the power spectrum measures the clustering of these galaxies (Amblard et al., 2011).

Another benefit to using angular power spectra, is that the data may be fit with a halo

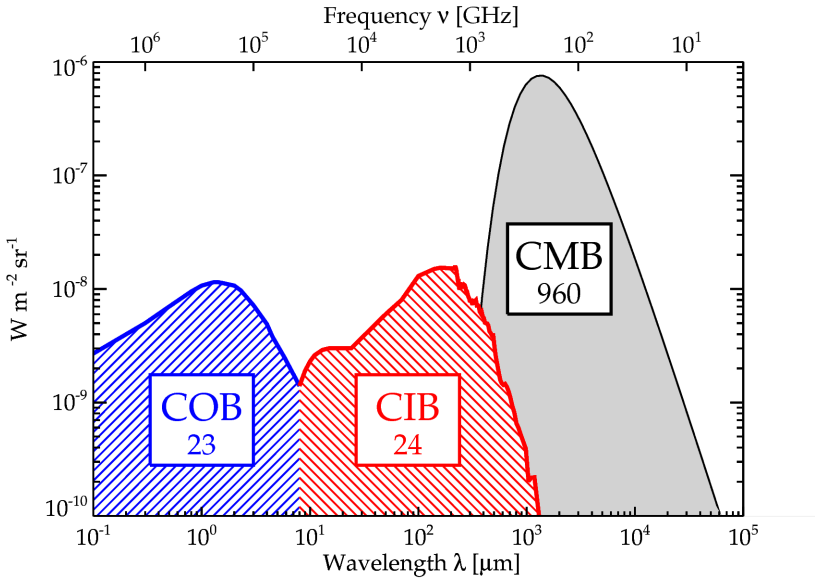

Figure 1.2: This figure from Dole et al. (2006) shows the energy as a function of wavelength of the cosmic optical background (COB), cosmic infrared background (CIB), and cosmic microwave background (CMB).

model in order to extract further meaning from the results. The halo model is a formalism for interpreting the clustering of dark matter. It is built upon the assumption that all dark matter resides in spheres, or halos, of differing size. When applying this to galaxies one also assumes that the galaxies occupy these dark matter halos and are so-called biased tracers of dark matter (Cooray & Sheth, 2002). Applying these models to power spectra has been quite successful (Thacker et al., 2013; Viero et al., 2013; Cooray et al., 2012; Zemcov et al., 2014).

The second chapter utilizes data from both *Spitzer* and *Herschel* probing the near and far-infrared, respectively. The CIB contains two peaks, one at near-IR wavelengths around 1 micron and the second at far-IR wavelengths around 250 microns (Dole et al., 2006) corresponding rougly to the wavelengths of these two telescopes. However, the emssision at near and far-IR are due to very different mechanisms. In the far-IR, the CIB is almost exclusively due to reprocessed thermal rediation of rest-frame UV light by cold dust. In the near-IR, however, the CIB is mostly composed of photons produced during nucleosythesis in stars and

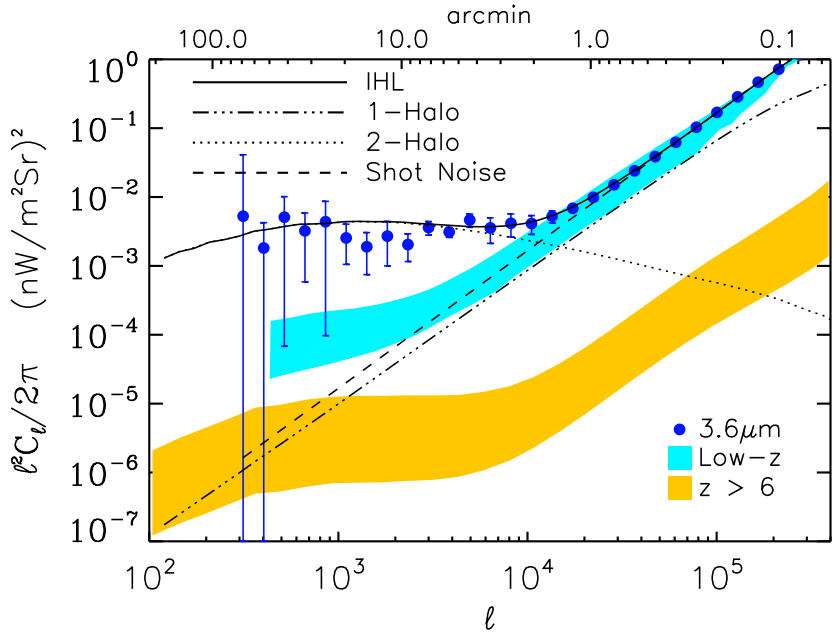

Figure 1.3: The angular power spectra of *Spitzer* 3.6 μm background anisotropies showing the different best fit models. Going through the data points is the intra-halo light model. The blue shaded region corresponds to low-z faint galaxies below the point source detection level. The yellow region coresponds to high-z sources including PopIII stars. Figure from Cooray et al. (2012).

a small component due to red-shifted UV light from high-z sources. In fact, there have been claims that the near-IR background anisotropies were mainly due to PopIII stars present during reionization (Kashlinsky et al. , 2005, 2007, 2012). Recent studies, however, find that such signals are not likely to be the dominant contribution (see Fig 1.3) and argue that that the signal is coming from low redshift and propose an origin associated with intra-halo light (Cooray et al., 2012; Zemcov et al., 2014). Intra-halo light involves diffuse stars that are tidally stripped during galaxy mergers and other interactions.

Chapter 2

H-ATLAS: The Cosmic Abundance of Dust from the Far-Infrared Background Power Spectrum

2.1 Introduction

While the total intensity of the cosmic far infrared background (CFIRB) is known from absolute photometry measurements (Puget et al., 1996; Fixen et al., 1998; Dwek et al., 1998), we still lack a complete knowledge of the sources, in the form of dusty star-forming galaxies, that make up the background. Limited by aperture sizes and the resulting source confusion noise (Nguyen et al., 2010), existing deep surveys with the *Herschel* Space Observatory [1] (Pilbratt et al. 2010) and ground-based sub-mm and mm-wave instruments resolve anywhere between 5 and 15% of the background into individual galaxies (Coppin et al., 2006; Scott et al., 2010; Oliver et al. , 2010; Clements et al., 2010; Berta et al., 2011). Anisotropies of the CFIRB, or

[1] *Herschel* is an ESA space observatory with science instruments provided by European-led Principal Investigator consortia and with important participation from NASA.

the spatial fluctuations of the background intensity, provide additional statistical information on the fainter galaxies, especially those that make up the bulk of the background.

While the fainter galaxies are individually undetected, due to gravitational growth and evolution in the large-scale structure these galaxies are expected to be clustered (Cooray et al., 2010; Maddox et al., 2010; Hickox et al., 2010; Kampen et al., 2012). In the ansatz of the halo model (Cooray & Sheth, 2002) such clustering of galaxies captures certain properties of the dark matter halos in which galaxies are found and the statistics of how those galaxies occupy the dark matter halos. The resulting anisotropies of the CFIRB are then a reflection of the spatial clustering of galaxies and their infrared luminosity. These CFIRB anisotropies, are best studied from the angular power spectrum of the background infrared light. Separately, statistics such as the probability of deflection, $P(D)$ (Glenn et al., 2010), probe the variance and higher order cumulant statistics of the intensity variations at the beam scale.

While early attempts to measure the angular power spectrum of the CFIRB resulted in low signal-to-noise measurements (Lagache et al., 2007; Viero et al., 2009), a first clear detection of the CFIRB power spectrum with *Herschel*-SPIRE (Griffin et al. 2010) maps between 30 arcseconds and 30 arcminute angular scales was reported in Amblard et al. (2011). Those first measurements also confirmed the interpretation that galaxies at the peak epoch of star formation in the Universe at redshifts of 1 to 3 trace the underlying dark matter halo distribution. Since then, additional measurements of the CFIRB power spectrum have come from Planck (Planck collaboration, 2011) and with additional SPIRE maps from the HerMES survey (Viero et al., 2013). With multiple fields spanning up to 20 deg^2, recent HerMES CFIRB power spectra probe angular scales of about 30 arcseconds: to 2°. The halo model interpretation of the HerMES spectra suggest that the halo mass scale for peak star-formation activity is $\log M_{\rm peak}/M_\odot \sim 13.9 \pm 0.6$ and the minimum halo mass to host dusty galaxies is $\log M_{\rm min}/M_\odot \sim 10.8 \pm 0.6$.

The angular power spectrum of CFIRB, in principle, captures the spatial distribution of the

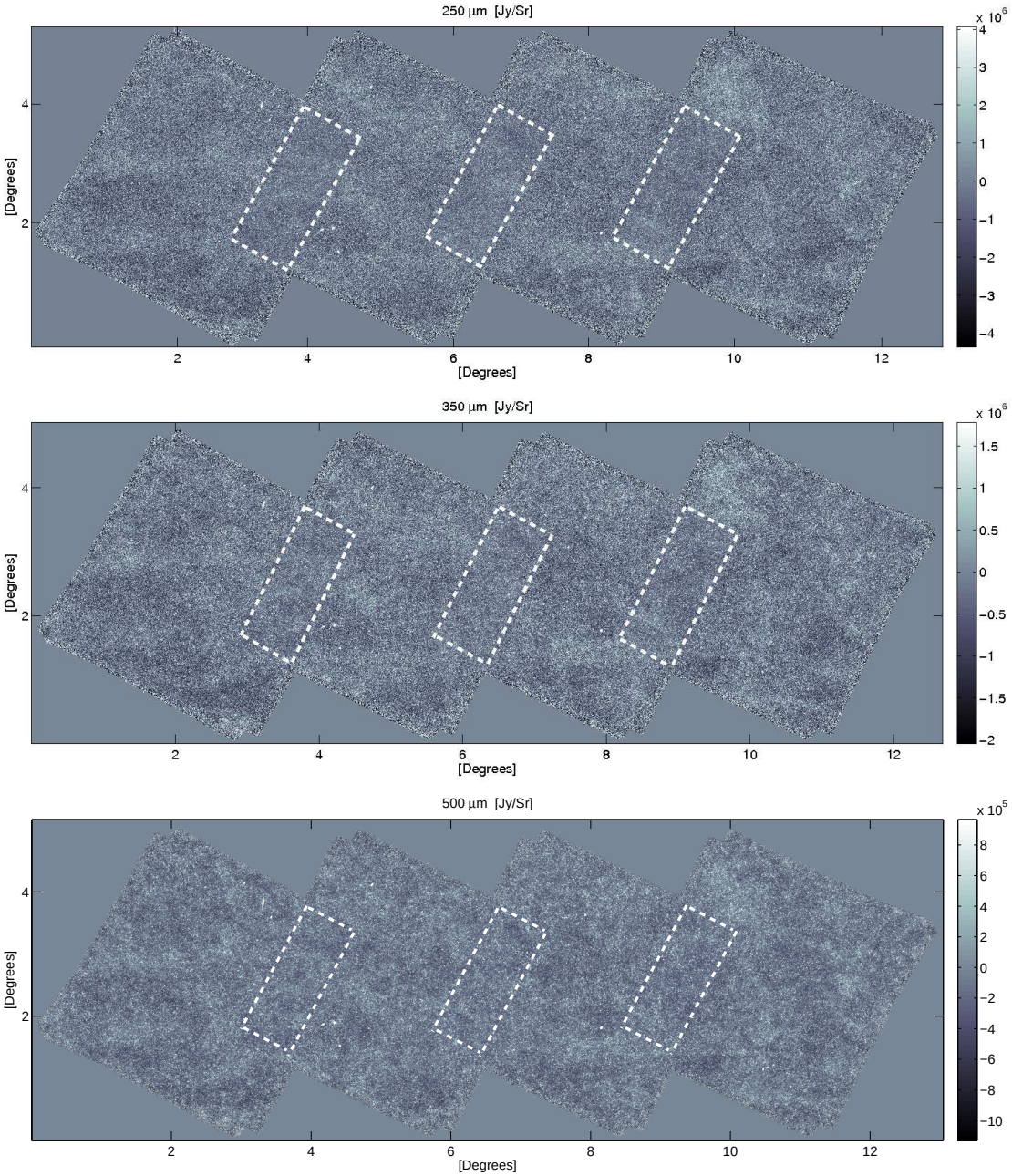

Figure 2.1: The *Herschel*-ATLAS GAMA-15 maps at 250 (top), 350 (middle) and 500 (bottom) μm with the three overlap regions used for the angular power spectrum measurements highlighted in dashed lines.

background intensity, regardless of whether the emission is from individual point sources or from smoothly varying diffuse sources, such as intracluster and intrahalo dust. Thus the angular power spectrum should be a sensitive probe of the total dust content in the Universe. The existing estimes of the dust abundance from direct emission measurements make use of the sub-mm luminosity (e.g., Dunne, Eales & Edmunds 2003) or dust mass (e.g., Dunne et al. 2011) functions, they are generally based out of extrapolations of the measured bright galaxy counts. The anisotropy power spectrum should capture the integrated emission from faint sources, especially at the flux density scale that dominate the confusion noise. Separately, other estimates of the cosmic dust abundance rely on the extinction of optical light, especially with measurements that combine magnification and extinction of quasars behind samples of foreground galaxies (Menard et al., 2010; Menard & Fukugita , 2012). It will be helpful to compare our direct emission measurement of the dust abundance with the extinction-based estimates since any differences can allow us to understand the important of galaxies with hot dust that could be missed in SPIRE maps. We make use of a halo model to interpret the anisotropy power spectrum with the goal of measuring $\Omega_{\rm dust}(z)$, the cosmic abundance of dust relative to the critical density, as a function of redshift.

To enable these measurements we make use of the wide field (~ 45 deg^2) maps of *Herschel*-ATLAS (Eales et al. 2010) in the three GAMA areas along the equator, and select a single area that has the least Galactic cirrus confusion. This GAMA-15 field involves 4 independent blocks of about 14 deg^2, each overlapping with the adjacent blocks by about 4 deg^2. We make use of the three overlap areas between the blocks to measure the power spectra at 250, 350 and 500 μm. The final power spectrum is the average of the individual power spectra of each of the overlapping regions. While this forces us to make a measurement over a smaller area than the total survey area, our power spectrum measurement has the advantage that with two sets of cross-linked scans we can make independent measurements of the noise power spectrum.

Our measurement approach is similar to that used for HerMES power spectra measurements (Amblard et al. 2011; Viero et al. 2012) using multiple scans to generate jack-knives of data to test the noise model. The total area used in HerMES measurements is about 12 and 60 deg^2, respectively, in Amblard et al. (2011) and Viero et al. (2012). However, H-ATLAS covers about 120 deg^2 in all three GAMA fields A measurement of the power spectrum in the whole of H-ATLAS GAMA areas requires an assumption about the noise power spectrum, since in regions with only one orthogonal scan or a single cross-linkeds scan, we are not able to separate the noise from the signal with data alone. In a future paper, we will present the power spectrum of the whole area using a noise model that is independently tested on various datasets to improve the confidence in separating noise in single cross-link scans. For now, we make use of two cross-link scans for cross-correlations and auto-correlations to separate noise and sky signal.

This paper is organized as follows. In Section 3.2.1, we briefly review how 250, 350 and 500 micron maps for the GAMA-15 field were constructed using HIPE (Ott, 2010) from raw time streams. In Section 3.2.3, we discuss how the auto and cross-correlation functions for each of the three fields were estimated, corrected, and assigned errors. The final power spectra are presented in Section 2.4. The halo model used to fit the data and the luminosity function is discussed in Section 3.3. Finally, in Section 2.6 & 2.7 we present our results and their implications, discuss future follow up work and give our concluding thoughts.

2.2 Map Making

For this work we generate SPIRE maps using the MADmap (Cantalupo et al, 2009) algorithm that is available within HIPE. The timeline data were reduced internally by the H-ATLAS team using HIPE version 8.2.0 (Pascale et al., 2011). The timelines were calibrated with corrections applied for the temperature-drift and deglitched both manually and auto-

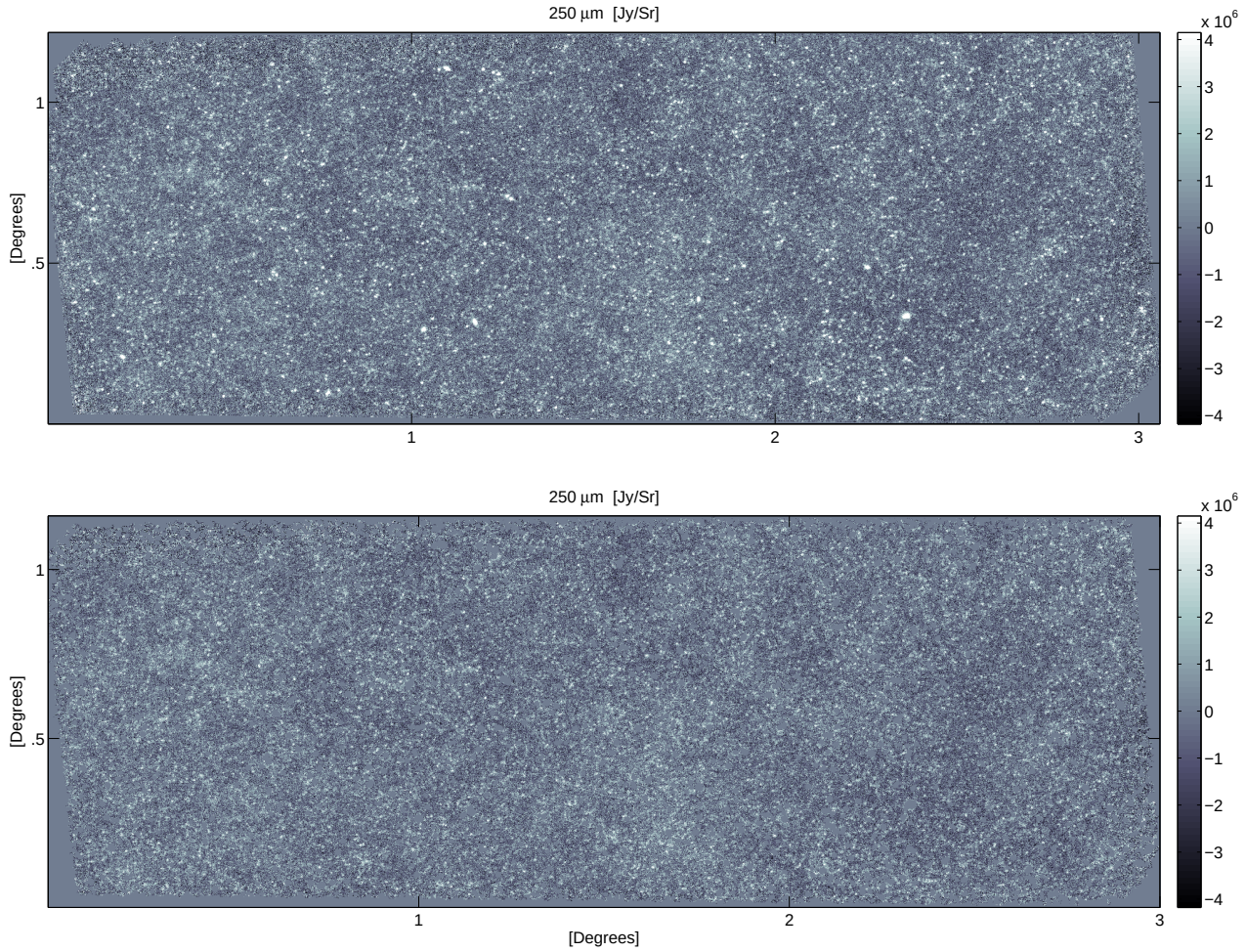

Figure 2.2: The left overlap region in Fig. 2.1 at 250 μm *Herschel*-ATLAS showing details of the background intensity variations without (top) and with (bottom) $S > 50$ mJy the bright source mask applied. This mask removes a substantial number of low-z bright galaxies detected in the areas used for the fluctuation study.

matically. Astrometry corrections were also applied to the timelines using offsets between SDSS sources and the cross-identifications (Smith et al., 2011). In addition, a scan-by-scan baseline polynomial remover was applied to remove gain variations leading to possible stripes.

The map-maker, MADmap, converts the timeline data $d(t)$

$$d(t) = n(t) + A(p,t) \times s(p)\,, \tag{2.1}$$

with noise $n(t)$ and sky signal $s(p)$, given the pointing matrix $A(p,t)$ between pixel and time domain to a map by solving the equation

$$m = (A^{\mathrm{T}} N^{-1} A)^{-1} A^{\mathrm{T}} N^{-1} d\,. \tag{2.2}$$

Here N is the time noise covariance matrix and m is the pixel domain maximum likelihood estimate of the noiseless signal map given N and d. We refer the reader to Cantalupo et al (2009) for more details of MADmap.

The final maps we use for this work consist of four partially overlapping tiles, each containing two sets of 96 scans in orthogonal directions (Fig. 2.1). The pixel-scale for the 250, 350 and 500 μm maps is 6 arcseconds, 8.333 arcseconds, and 12 arcseconds, respectively, corresponding to 1/3 of the beam size.

In regions where the tiles do not overlap, the map at each wavelength consists of a single scan each in the two orthogonal scan directions. In the overlap region, we have two scans in each direction. As discussed below, we are able to estimate the noise and signal power spectra independent of each other using the auto-correlations of the combined 4-scan map and the cross-correlations involving various jack-knife combinations. In Fig. 2.2 we show an example overlap region.

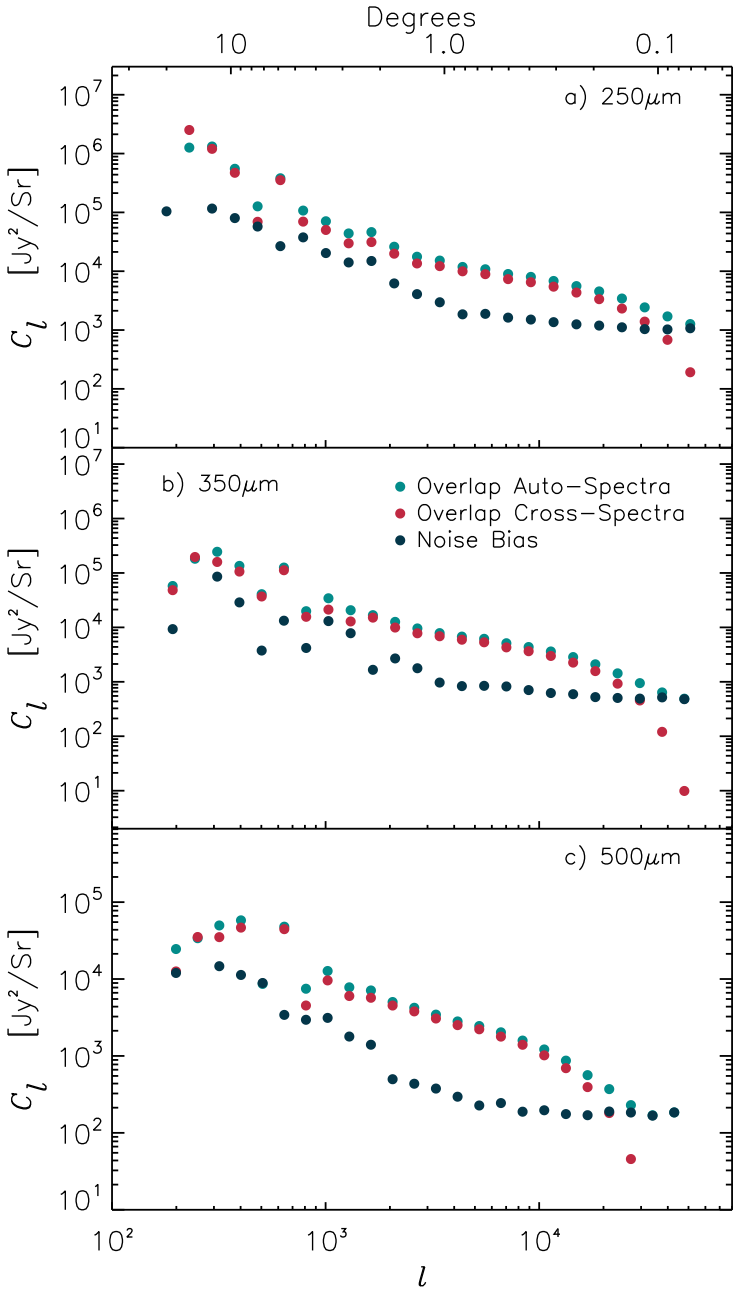

Figure 2.3: The raw C_l of the GAMA-15 overlap regions at 250 (top), 350 (middle) and 500 (bottom) μm, respectively. The green points show the auto-power spectra computed from overlap regions using all 4 scans. This power spectrum is a combination of the real sky anisotropy power spectrum and the instrumental noise. We estimate the sky signal independent of noise by creating two sets of maps for each of the three overlap regions with two orthogonal scans each and then taking the cross power spectrum (red points) of those independent maps. The difference of these two spectra shows the instrumental noise power spectrum (black points).

2.3 Power Spectra

We now discuss the measurement of angular anisotropy power spectra in each of the three SPIRE bands. To be consistent with previous measurements of the SPIRE angular power spectrum (Amblard et al., 2011) our maps are masked by taking a 50 mJy/beam flux cut and then convolving with the point response function. Such a flux cut, through a mask that removes the bright galaxies, also minimizes the bias coming from those bright sources by reducing shot-noise effects. The same mask also includes a small number of pixels that do not contain any useful data, either due to scan strategy or data corruption. The combined mask removes roughly 13, 12 and 15% of the pixels at 250, 350 and 500 μm, respectively. The fractions of masked pixels are substantially higher than the fractions of Amblard et al. (2011) of 1 to 2% as the ATLAS GAMA-15 field has a large density of $z < 0.1$ spiral galaxies over its area relative to more typical extragalactic fields used in the Amblard et al. (2011) study. These galaxies tend to be brighter, especially at 250 μm. While the fraction masked is larger, the total number of pixels used for this study is comparable to Amblard et al. (2011) with 2.9×10^6, 1.5×10^6 and 7.0×10^5 at 250, 350 and 500 microns in each of the three overlap regions.

To measure the power spectrum in the final set of maps, we make use of 2D Fourier transforms. In general this is done with masked maps of the overlap regions, denoted M_1 and M_2 in real space. If we denote the 2D Fourier transform of each map as $\widetilde{M_1}$ and $\widetilde{M_2}$, the power spectrum, C_l, formed for a specific l bin between between l-modes l_1 and l_2, is the mean of the squared Fourier modes $\tilde{M}_1\tilde{M}_2^*$ between l_1 and l_2. The same can be used to describe the auto power spectra, but with $M_1 = M_2$.

The raw power spectra are summarized in Fig. 2.3. Here, we show the auto spectra in the total map, as well as the cross spectrum with maps made with half of the time-ordered data in each map. The difference of the two provides us with an estimate of the instrumental noise.

At small angular scales (large ℓ values) the noise follows a white-noise power spectrum, with C_l equal to a constant. At large angular scales, the detectors show the expected $1/f$-type of noise behavior, with the noise power spectrum rising as $C_l \propto l^{-2}$. We fit a model of the form

$$N_l = N_0 \left[\left(\frac{l_0}{l} \right)^2 + 1 \right] , \tag{2.3}$$

and determine the knee-scale of the $1/f$ noise and the amplitude of noise power spectra. The noise values are $N_0 = 1.2 \times 10^3, 5.3 \times 10^2$ and 1.8×10^2 Jy^2/sr at 250, 350 and 500 μm, comparable to the detector noise in the 4-scan maps of the Lockman-hole used in Amblard et al. (2011). The knee at which $1/f$ noise becomes important is $l_0 = 3730, 2920$ and 3370, comparable to the expected knee at a wavenumber of 0.15 arcmin^{-1} given the scan rate and the known properties of the detectors (Griffin et al., 2010).

The raw spectra we have computed directly from the masked maps are contaminated by several different effects that must be corrected for. These issues are: the resolution damping from the instrumental beam, the filtering in the map-making process, and the fictitious correlations introduced by the bright source and corrupt pixel mask. Including these effects, we can write the measured power spectrum as

$$C'_l = B^2(l) T(l) M_{ll'} C_{l'} , \tag{2.4}$$

where C'_l is the observed power spectrum from the masked map, $B(l)$ is the beam function measured in a map, $T(l)$ is the map-making transfer function, and $M_{ll'}$ is the mode coupling matrix resulting from the mask. Here, $C_{l'}$ is the true sky power spectrum and is determined by inverting the above equation.

We now briefly discuss the ways in which we either determine or correct for the effects just outlined.

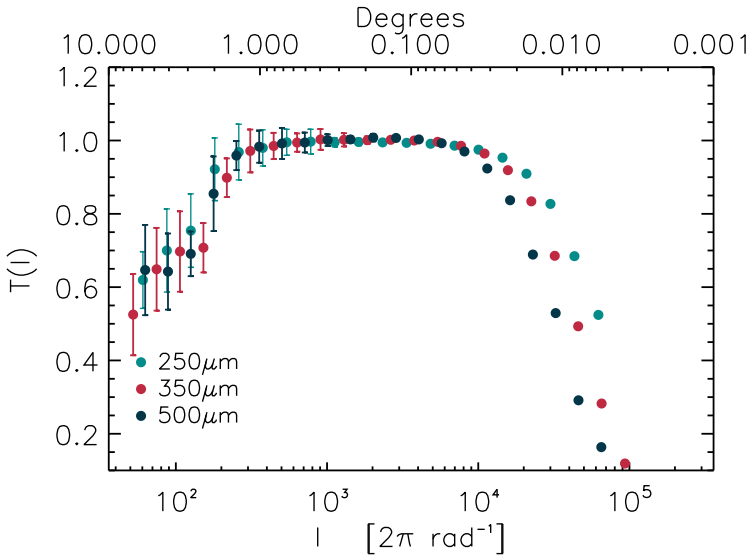

Figure 2.4: Map-making transfer function $T(l)$ for the MADmap map making tool used for the GAMA-15 field anisotropy power spectrum measurement. The uncertainties in the transfer function are calculated from 100 random realizations of the sky as described in Section 3.1.

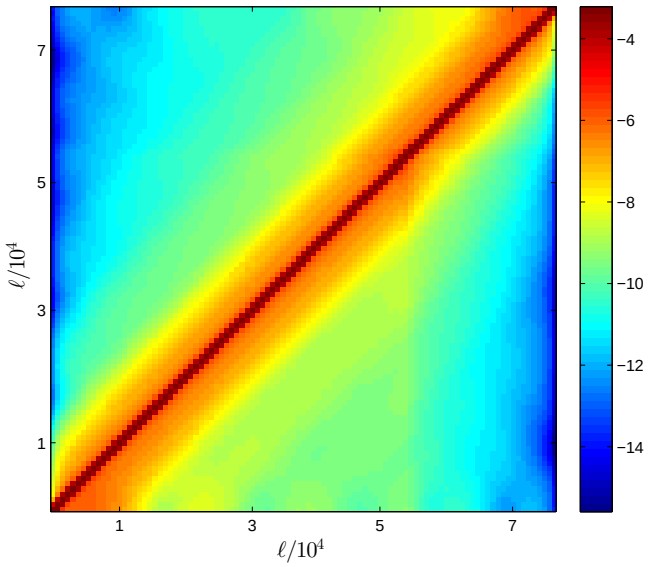

Figure 2.5: An example inverse-mode coupling matrix $M_{ll'}^{-1}$ for one of the overlap regions (log scale).

2.3.1 The Map-Making Transfer Function

Due to the finite number of detectors, the scan pattern, and the resulting analysis technique to convert timeline data into a map, the map we produce is not an exact representation of the sky. The modifications are associated with the map-making process, relative to the true sky, are described by the transfer function $T(l)$. We determine this by making 100 random realizations of the sky using Gaussian random fields derived from a first estimate of the H-ATLAS power spectrum. We sample those skies using the same timeline data as the actual observations and analyze the simulated timelines with the same data reduction and map-making HIPE scripts for the actual data. We then compute the average of the ratio between the estimated power spectra and the input spectrum. This function is then the transfer function associated with polynomial filtering and the map-making process. This transfer function, like the beam, represents a multiplicative correction to the data. We divide the estimated power spectrum of the data by this transfer function to remove the map-making pipeline processing effects.

In Fig. 3.7 we show the transfer functions at 250, 350 and 500 μm with 68% error bars taken from the standard deviation of 100 simulations. The transfer function is such that it turns over from 1 at both large angular scales, corresponding to roughly the scale of an individual scan length, and the beam scale. The large-scale deviation, which is wavelength independent, is due to the polynomial removal from each timeline of data, while the turnover at small angular scales is due to the cut-off imposed by the instrumental point response function or the beam. The transfer function is more uncertain at the large angular scales due to the finite number of simulations and the associated cosmic variance resulting from the field size. Given its multiplicative nature, errors from this transfer function are added in quadrature with rest of the errors.

2.3.2 The Beam

Following Amblard et al. (2011), the beam function is derived from Neptune observations of SPIRE. The Neptune timeline data are analyzed with the same pipeline and our default map maker in HIPE. The resulting beam functions are similar to those of Amblard et al. (2011) and we find no detectable changes resulting from the two different map makers between this work and the SMAP (Levenson et al., 2010) pipeline of the SPIRE Instrument Team used in Amblard et al. (2011) and Viero et al. (2012). This is primarily due to the fact that the beam measurements involve a large number of scans and Neptune is several orders of magnitude brighter than the extragalactic confusion noise. We interpolate the beam function measured from Neptune maps in the same ℓ modes at which we compute our anisotropy power spectra. This beam transfer function, $B(l)$, at each of the wavelengths represents a multiplicative correction to the data. Similar to Amblard et al. (2011), we compute the uncertainty in the beam function by computing the standard deviation of several different estimates of the beam function by subdividing the scan data to 4 different sets. The error on the beam function in Fourier space is propagated to the final error and is added in quadrature with rest of the errors.

2.3.3 Mode-Coupling Matrix

The third correction we must make to the raw power spectrum involves the removing of fictitious correlations between modes introduced by the bright sources and contaminated or zero-data pixel mask. Due to this mask the 2D Fourier transforms are measured in maps with holes in them. In the power spectrum these holes result in a Fourier mode coupling that biases the power spectrum lower at large angular scales and higher at smaller angular scales. This can be understood since the modes at the largest angular scales, like the mean of the map, are broken up into smaller scale modes with any non-trivial mask.

To correct for the mask we make use of the method used in Cooray et al. (2012). The method involves capturing the effects of the mask on the power spectrum into a mode-coupling matrix $M_{ll'}$. The inverse of the mode coupling matrix then removes the contamination and corrects the raw power spectrum to a power spectrum that should be measurable in an unmasked sky. The correction both restores the power back to the large angular scale modes by shifting the power away from the small angular scale modes, especially those at the modulation scale introduced by the mask.

To generate $M_{ll'}$ we apply the mask to a map consisting of a Gaussian realization of a single l-mode and take the power spectrum of the resulting map. This power spectrum represents the shuffling of power the mask performs on this specific l-mode among the other l-modes. This process is repeated for all l-modes and these effects of the mask on each mode are then stored in a matrix. This matrix, $M_{ll'}$ now represents the transformation from an unmasked to a masked sky by construction. By inverting this matrix, shown in Fig. 5, we are left with the transformation from a masked to an unmasked sky removing the fictitious couplings induced by the mask applied to the raw power spectra. The matrix $M_{ll'}$ behaves such that in the limit of no $l-$mode coupling $M_{ll'} = f_{\rm sky}\delta_{ll'}$ where $f_{\rm sky}$ is the fraction of the sky covered. Thus in the limit of partial sky coverage the correction becomes the standard formula with $C_l' = f_{\rm sky}C_l$. For more details, including figures demonstrating the robustness of the method, we refer the reader to Cooray et al. (2012).

2.4 Power Spectrum Results

The final power spectrum C_l at each of the three wavelengths is shown in Fig.**??** and 2.7. The final error bars account for the uncertainties associated with the (a) beam, (b) map making transfer function, (c) instrumental or detector noise (Fig. 2.3), and the cosmic variance associated with the finite sky coverage of the field. In Fig. 2.7 we compare these final H-ATLAS

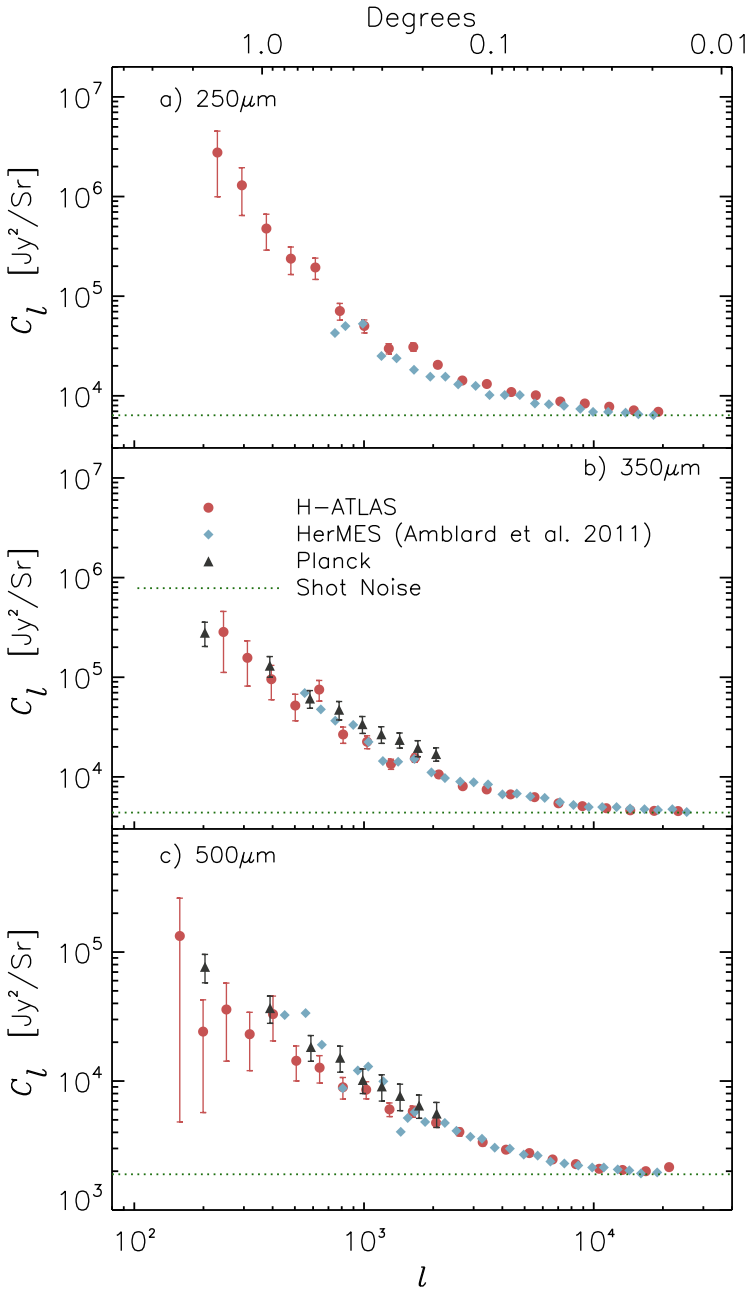

Figure 2.6: Final angular power spectra of CFIRB anisotropies in the H-ATLAS GAMA-15 field at 250 (top), 350 (middle) and 500 (bottom) μm. The power spectra are plotted as C_l prior to the removal of the shot-noise term. Here we compare the power spectra measured with H-ATLAS data to Planck and previous *Herschel* results from HerMES. Due to the high cirrus fluctuation amplitude and clustering, the H-ATLAS power spectrum in the GAMA-15 field at 250 μm is higher than the existing HerMES results, while the measurements are generally consistent at 350 and 500 μm.

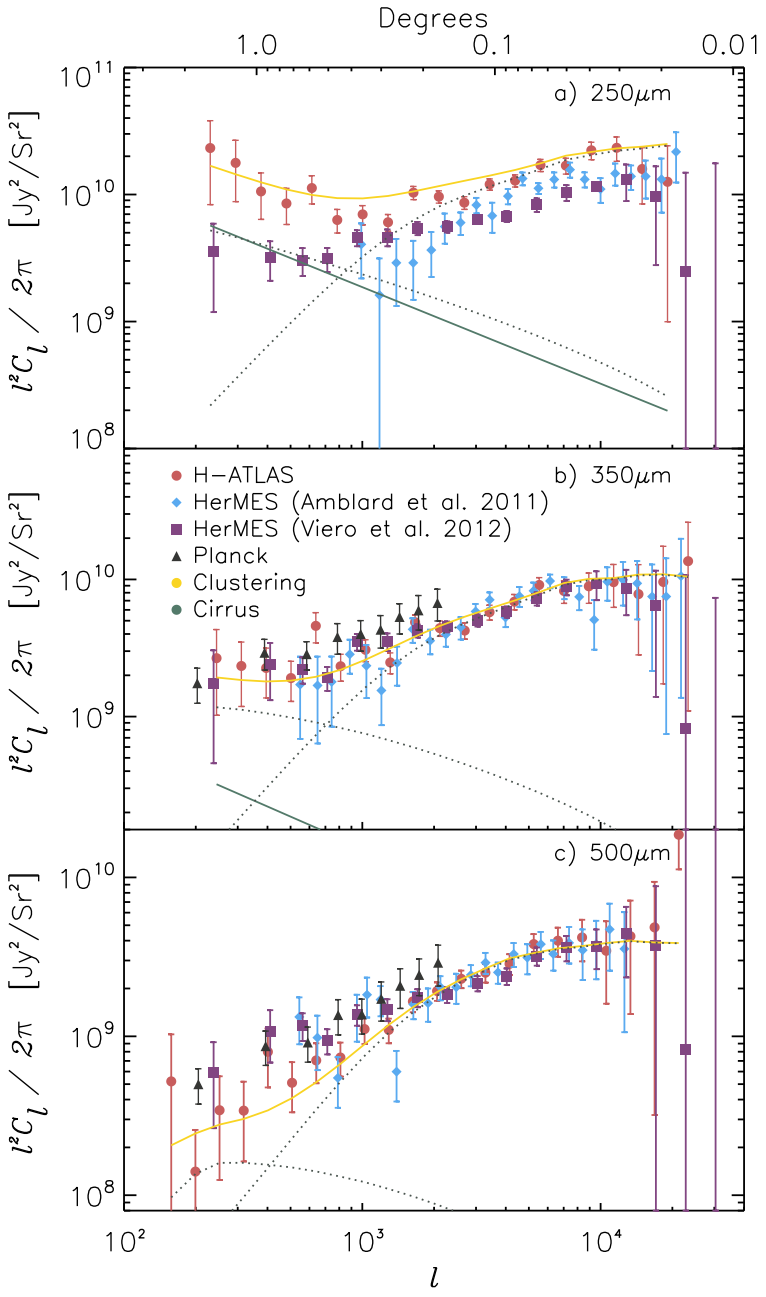

Figure 2.7: Final angular power spectra of CFIRB anisotropies in the H-ATLAS GAMA-15 field at 250 (top), 350 (middle) and 500 (bottom) μm. We show the power spectra as $l^2C_l/2\pi$ after removing the shot-noise level at each of the wave bands. We add the uncertainty associated with the shot-noise level back to the total error budget in quadrature. This results in the increase in errors at high multipoles or small angular scales. The curves show the best-fit model separated into 1 and 2-halo terms (see text for details) and the total (orange line). The solid line that scales roughly as $l^2C_l \sim l^{-0.9}$ is the best-fit Galactic cirrus fluctuation power spectrum. Due to the high cirrus fluctuation amplitude and clustering, the H-ATLAS power spectrum in the GAMA-15 field at 250 μm is higher than the existing HerMES results, while the measurements are generally consistent at 350 and 500 μm.

GAMA-15 power spectra with measurements of the CFIRB anisotropy power spectrum measurements from HerMES (Amblard et al. 2011) and Planck (Planck collaboration 2011) team measurements. We find general agreement, but we also find some differences. At 250 μm, we find the amplitude to be larger than the existing SPIRE measurements of the power spectrum at 250 μm in HerMES while the measurements are more consistent at 350 and 500 μm. We attribute this increase to the wide coverage of H-ATLAS and the presence of a large surface density of galaxies at low redshifts. While most of these galaxies are masked we find that the fainter population likely remains unmasked and contributes to the increase in the power that we have seen. This conclusion is also consistent with the strong cross-correlation between detected SPIRE sources in GAMA fields of H-ATLAS and the SDSS redshift survey (e.g., Guo et al. 2011). The difference between *Herschel*-SPIRE measurements and Planck measurements are discussed in Planck collaboration (2011) and we refer the reader to that discussion. We continue to find differences between our measurements and Planck power spectra at 350 μm, even with Planck data corrected for the frequency differences and other corrections associated with the source mask, as discussed in Planck collaboration (2011).

Note that the power spectra in the left panels of Fig. **??** asymptote to a $C_l \sim$ constant. This is the shot-noise coming from the Poisson behavior of the sources. In Fig. 2.7 we show the final power spectra plotted as $l^2 C_l / 2\pi$, with the Poisson noise removed at each band. They now reveal the underlying clustering of submillimeter galaxies. With sources masked down to 50 mJy, our shot-noise amplitudes are 6700 ± 140, 4400 ± 130 and 1900 ± 90 Jy^2/sr at 250, 350 and 500 μm, respectively (see Table 1). We determine the Poisson noise uncertainties based on the overall fit to C_l measurements at the three highest ℓ-bins.

For comparison to our shot-noise values, the shot-noise values of Amblard et al. (2011) are 6100 ± 120, 4600 ± 70 and 1800 ± 80 Jy^2/sr at 250, 350 and 500 μm, respectively. While the shot-noise values are consistent at 350 and 500 μm, we find an increased shot-noise amplitude at 250 μm, consistent with the higher amplitude of the clustering part of the power spectrum.

In addition to Planck and Amblard et al. (2011) HerMES measurements, in Fig. 2.7 we also compare our measurements to more recent Viero et al. (2012) HerMES measurements. At 350 and 500 μm the difference between all of Herschel-SPIRE measurements and Planck is clear.

At 250 μm, we find that our measurements have a higher amplitude at all angular scales relative to previous SPIRE measurements. At large angular scales, we find that the increase is coming from the higher intensity of cirrus in our GAMA-15 fields (Bracco et al. 2011). The cirrus properties as measured from the power spectra are discussed in Section 6.1. As part of the discussion related to our results on the galaxy distribution that is contributing the far-IR background power spectrum (Section 6.2), we will explain the difference between the HerMES and H-ATLAS power spectrum at 250 μm as due to an excess of low-redshift galaxies in the H-ATLAS GAMA-15 field (Rigby et al. in prep). The measurements shown in Fig. 2.7 constitute our final CFIRB power spectrum measurements in the H-ATLAS GAMA-15 field. These power spectra values are tabulated in Table 2. We now discuss the model used for the interpretation leading to the best-fit model lines shown in Fig. 2.7.

2.5 Halo Modeling of the CFIRB Power Spectrum

To analyze the H-ATLAS GAMA-15 power spectra measurements we implement the conditional luminosity function (CLF) approach of Giavalisco & Dickinson (2001); Lee et al. (2009); De Bernardis & Cooray (2012). We recall below the main features of the model and refer the reader to these works for more details. The goal is to work out the relation between IR luminosity and halo masses of the galaxies that are contributing to the CFIRB power spectrum. We populate halos with the best-fit $L_{\rm IR}(M)$ relation from the data and use that to determine the abundance of dust ($\Omega_{\rm dust}$) in the Universe. The CLF approach proposed here improves over several assumptions that were made in Amblard et al. (2011) to interpret

the first Herschel-SPIRE anisotropy power spectrum measurements.

First, the probability density for a halo or a sub-halo of mass M to host a galaxy with IR luminosity L is modeled as a normal distribution with:

$$P(L|M) = \frac{1}{\sqrt{2\pi}\sigma_L(M)} \exp\left[-\frac{(L-\bar{L}(M))^2}{2\sigma_L(M)^2}\right] . \tag{2.5}$$

The relation between the halo mass and the average luminosity $\bar{L}(M)$ is expected to be an increasing function of the mass with a characteristic mass scale M_{0l} and we can write (see Lee et al. (2009))

$$\bar{L}(M) = L_0 \left(\frac{M}{M_{0l}}\right)^{\alpha_l} \exp\left[-\left(\frac{M}{M_{0l}}\right)^{-\beta_l}\right] . \tag{2.6}$$

As already discussed by Lee et al. (2009) these parameterizations do not have a specific physical motivation, except for the requirement that the luminosity increases as an increasing function of the halo mass and offer the advantage that one can explore a large range of possible shapes for the luminosity-mass relation. While there is no motivation to use this specific form over another, certain models of galaxy formation do predict a $L(M,z)$ relation and our results based out of the model-fits to CFIRB power spectrum can be compared to those model predictions. In particular, the model of Lapi et al. (2011) predicts $L(M,z) \propto M(1+z)^{2.1}$, while the cold-flow accretion model of Dekel et al. (2009) predicts $L(M,z) \propto M^{1.15}(1+z)^{2.25}$.

The total halo mass function is given by the number density of halos or sub-halos of mass M. The contribution of halos $n_h(M)$ is taken to be the Sheth & Tormen relation (Sheth & Tormen, 1999). The sub-halos term can be modeled through the number of sub-

halos of mass m inside a parent halo of mass M_p, $N(m|M_p)$. The total mass function is then written as

$$n_T(M) = n_h(M) + n_{sh}(M)\,, \tag{2.7}$$

where $n_{sh}(M)$ is the sub-halo mass function

$$n_{sh}(M) = \int N(M|M_p) n_h(M_p) dM_p\,. \tag{2.8}$$

Here we parameterize $N(m|M)$ following the semi-analytical model of van de Bosch et al. (2005).

Neither the normalization nor the slope of the sub-halo mass function are universal and both depend on the ratio between the parent halo mass and the non-linear mass scale, M_*. M_* is defined as the mass scale where the rms of the density field $\sigma(M, z)$ is equal to the critical over-density required for spherical collapse $\delta_c(z)$. The contribution of central galaxies to the halo occupation distribution (HOD) is simply the integral of $P(L|M)$ over all luminosities above a certain threshold L_0, either fixed by the survey or a priori selected so that

$$\langle N_c(M)\rangle_{L\geq L_{min}} = \int_{L_{min}} P(L|M) dL\,, \tag{2.9}$$

which, in the absence of scatter, reduces to a step function $\Theta(M-M_0)$, as expected. Note that all integrals over the luminosity L also have a redshift-dependent cut-off at the upper limit corresponding to the flux cut of 50 mJy that we used for the power spectrum measurement.

Table 2.1: Parameter values from MCMC fits to the H-ATLAS GAMA-15 angular power spectra at 250, 350 and 500 μm.

HOD	α_l	0.69 ± 0.04
	β_l	0.09 ± 0.05
	$\log(L_0/L_\odot)$	9.52 ± 0.08
	$\log(M_0/M_\odot)$	11.5 ± 1.7
	P_M	-2.9 ± 0.4
CFIRB SED	$T_{\rm dust}$	37 ± 2 K
	$\beta_{\rm dust}$	unconstrained
Cirrus	$C_{250}^{l=230}$	$3.5 \pm 1.3 \times 10^5$ Jy^2/sr
	$C_{350}^{l=230}$	$1.2 \pm 1.0 \times 10^4$ Jy^2/sr
	$C_{500}^{l=230}$	$1.1 \pm 0.9 \times 10^3$ Jy^2/sr
	$T_{\rm cirrus}$	21.1 ± 1.9 K
	$\beta_{\rm cirrus}$	2.9 ± 0.8
Poisson	SN_{250}	6700 ± 140 Jy^2/sr
	SN_{350}	4400 ± 130 Jy^2/sr
	SN_{500}	1900 ± 90 Jy^2/sr

For the satellite galaxies, the HOD is related to the sub-halos

$$\langle N_s(M)\rangle_{L\geq L_{min}} = \int_{L_{min}} dL \int dm N(m|M)P(L|m)\,. \tag{2.10}$$

The total HOD is then

$$\langle N_{\rm tot}(M)\rangle_{L\geq L_{min}} = \langle N_h(M)\rangle_{L\geq L_{min}} + \langle N_{sh}(M)\rangle_{L\geq L_{min}}\,. \tag{2.11}$$

We account for the possible redshift evolution of the luminosity-halo mass relation by intro-

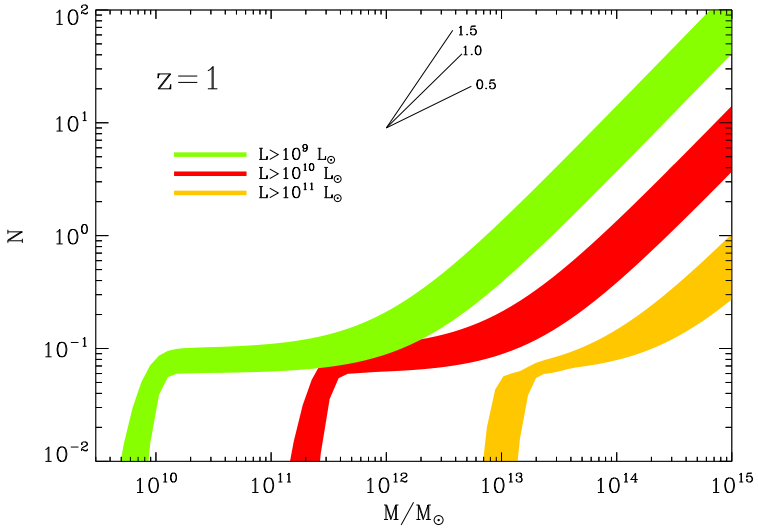

Figure 2.8: Best-fit halo occupation distribution and the 1σ range at $z = 1$ for three cases involving $L_{\rm IR} > 10^9, 10^{10}$ and 10^{11} $L_\odot$. The three lines to the top show the different power-laws for comparison with the shape of the HOD. The satellite galaxies contribution has a slope ~ 1 when $L_{\rm IR} \sim 10^9$ $L_\odot$.

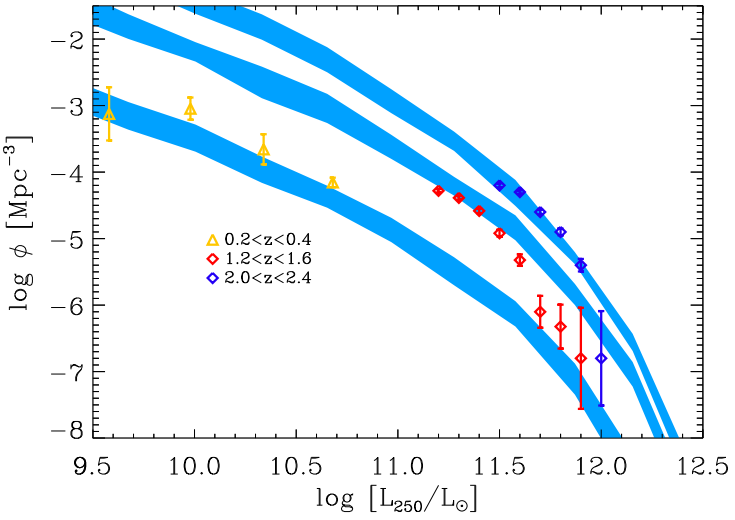

Figure 2.9: Luminosity functions predicted by our model compared to data from Eales et al. (2010) ($0.2 < z < 0.4$) and Lapi et al. (2011) ($1.2 < z < 1.6, 2 < z < 2.4$). The shaded region corresponds to the 68% confidence level.

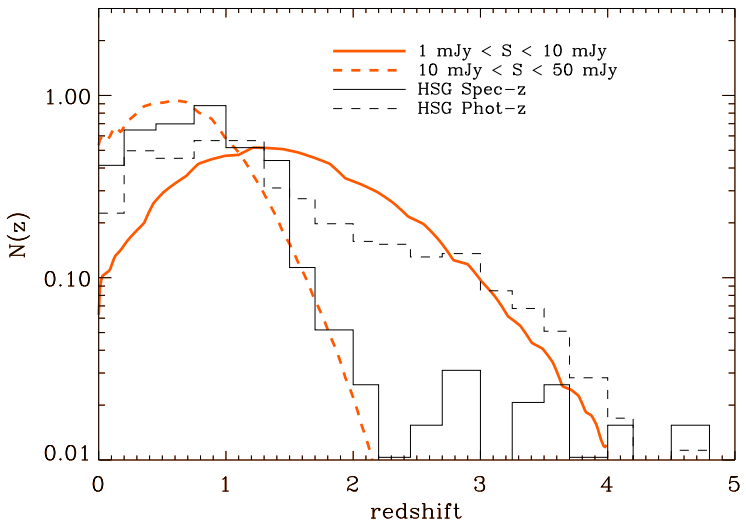

Figure 2.10: Normalized redshift distributions of FIR-bright galaxies predicted by our model for two different flux density cuts at 250 μ (thick solid line for $1\,\mathrm{mJy} < S < 10\,\mathrm{mJy}$ and thick dashed line for $10\,\mathrm{mJy} < S < 50\,\mathrm{mJy}$). For comparison in corresponding thin lines we show the measured redshift distributions for the Herschel-selected galaxies (HSGs) at the same flux density bins with optical spectra in Casey et al. (2012).

ducing the parameter p_M and rewriting the mass scale M_{0l} as:

$$M_{0l}(z) = M_{0l,z=0}(1+z)^{p_M}\,. \tag{2.12}$$

Under the assumption that the central galaxy is at the center of the halo and that the halo radial profile of satellite galaxies within dark matter halos follow that of the dark matter, given by the Navarro, Frenk and White (NFW) profile (Navarro et al., 1997), we can write the 1-halo and 2-halo terms of the three-dimensional power spectrum:

$$P^{1h}(k) = \frac{1}{n_g^2}\int dM \langle N_T(N_T-1)\rangle u(k,M)^p n_h(M)\,, \tag{2.13}$$

where $u(k, M)$ is the NFW profile in Fourier space and n_g is the galaxy number density

$$n_g = \int dM \langle N_g(M) \rangle n_h(M) \,. \tag{2.14}$$

The second moment of the HOD that appear in eq. 2.13 can be simplified as

$$\langle N_T(N_T - 1) \rangle \simeq \langle N_T \rangle^2 - \langle N_h \rangle^2 \,, \tag{2.15}$$

and the power index p for the NFW profile is $p = 1$ when $\langle N_T(N_T - 1) \rangle < 1$ and $p = 2$ otherwise (Lee et al. , 2009).

The two-halo term of galaxy power spectrum is

$$\begin{aligned} P^{2h}(k) &= \left[\frac{1}{n_g} \int dM \langle N_T(M) \rangle u(k, M) n_h(M) b(M) \right]^2 \\ &\quad \times P_{\rm lin}(k) \,, \end{aligned} \tag{2.16}$$

where $P_{\rm lin}(k)$ is the linear power spectrum and $b(M)$ is the linear bias factor calculated as in (Cooray & Sheth, 2002). The total galaxy power spectrum is then $P_g(k) = P^{1h}(k) + P^{2h}(k)$.

The observed angular power spectrum can be related to the three-dimensional galaxy power spectrum through a redshift integration along the line of sight (Knox et al., 2001; Amblard & Cooray, 2007):

$$C_\ell^{\nu\nu'} = \int dz \left(\frac{d\chi}{dz} \right) \left(\frac{a}{\chi} \right)^2 \bar{j}_\nu(z) \bar{j}_{\nu'}(z) P_g(\ell/\chi, z) \,, \tag{2.17}$$

where χ is the comoving radial distance, a is the scale factor and $\bar{j}_\nu(z)$ is the mean emissivity at the frequency ν and redshift z per comoving unit volume that can be obtained as:

$$\bar{j}_\nu(z) = \int dL\phi(L,z)\frac{L}{4\pi}\,. \tag{2.18}$$

Here the luminosity function is

$$\phi(L,z)dL = dL\int dMP(L|M)n_T(M,z)\,. \tag{2.19}$$

To fit data at different frequencies we assume that the luminosity-mass relation in the IR follows the spectral energy distribution (SED) of a modified black-body (here we normalize at $250\mu m$ at $z=0$) with

$$L_\nu(M) = L_{250}(M)\frac{(1-e^{-\tau})B(\nu_0,T_d)}{(1-e^{-\tau'})B(250,T_d)}\,, \tag{2.20}$$

where T_d is the dust temperature, the optical depth is $\tau = \left(\frac{\nu_0}{\nu}\right)^{\beta_d}$, $\tau' = \tau(\nu_0 = 250)$, $B(\nu_0,T_d)$ is the Planck function and $L_{250}(M)$ is given by eq (2.6).

The final power spectrum is a combination of galaxy clustering, shot-noise and the Galactic cirrus such that $C_l^{\rm tot} = C_l^{\rm CFIRB} + C_l^{\rm cirrus} + C_l^{\rm SN}$, where $C_l^{\rm CFIRB}$ is the power spectrum derived above and $C_l^{\rm SN}$ is the scale-independent shot-noise. To account for the Galactic cirrus contribution to the CFIRB, we add to the predicted angular power spectrum a cirrus power-law power spectrum with the same shape of that used by Amblard et al. (2011), where the authors assumed the same cirrus power-law power-spectrum shape from measurements of IRAS and MIPS (Lagache et al., 2007) at $100\,\mu$m with $C_l \propto l^{-n}$ with $n = 2.89 \pm 0.22$. In

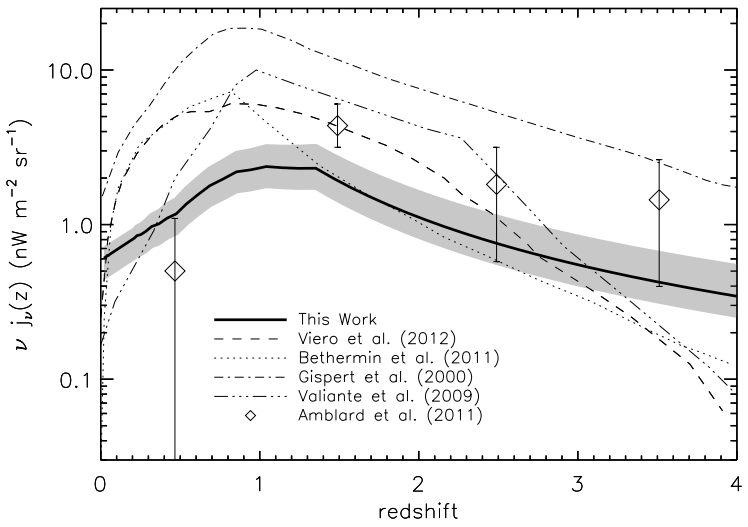

Figure 2.11: Best-fit determination of mean emissivity at 250 μm as a function of the redshift, $\nu j_\nu(z)$ (thick solid line), and its 1σ error from the MCMC model fits (grey shaded region) for sources with $S_{250} < 50$mJy. We show several model predictions from the literature (Valiante et al., 2009; Bethermin et al., 2011) and compare our estimates to the determinations from the halo model fits to the CFIRB power spectra by Amblard et al. (2011) and Viero et al. (2013). Amblard et al. (2011) measurements involve a binned description of $j_\nu(z)$ with 1σ errors determined from the fit, while Viero et al. (2013) result is the best-fit relation for their work.

Amblard et al. (2011) this 100 μm spectrum was extended to longer wavelengths using the spectral dependence of Schlegel (1998). Here we rescale the amplitude of the cirrus power spectrum with amplitudes $C_i^{\rm cirrus}$ at each of the three wavelengths ($i = 250, 350$ and 500 μ) taken to be free parameters and model-fit those three parameters describing the amplitude as part of the global halo model fits with the MCMC approach.

2.6 Results and Discussion

We fit the halo-model described above to the 250, 350 and 500 μm CFIRB angular power spectrum data for the H-ATLAS GAMA-15 field by varying the halo model parameters and the SED parameters. The dimension of the parameter space is thus 12 with free pa-

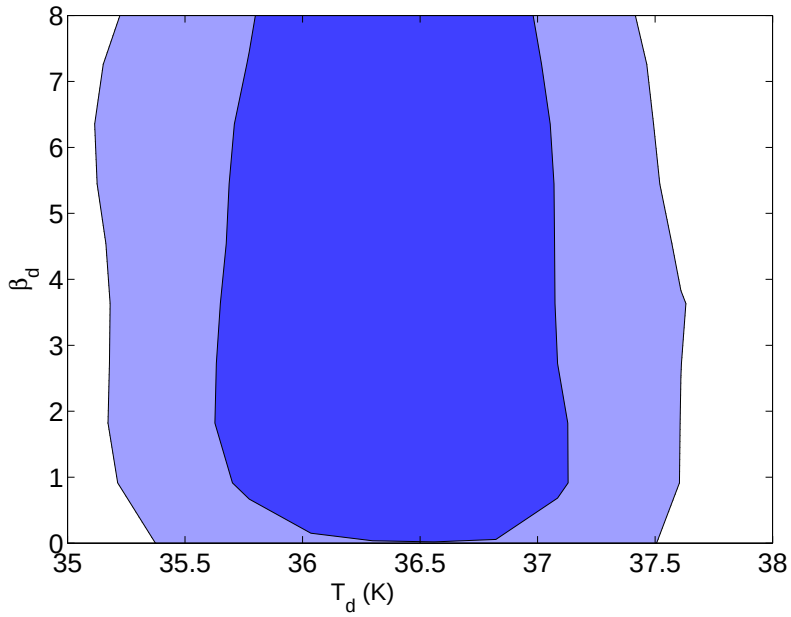

Figure 2.12: 68% and 95% confidence level constraints on T_d and $\beta_{\rm dust}$.

rameters involving T_d, β_d, α_l, β_l, L_0, p_M, $C_i^{\rm cirrus,l=230}$ and SN_i. We make use of a Markov Chain Monte Carlo (MCMC) procedure, modified from the publicly available CosmoMC (Lewis & Bridle, 2002), with a convergence diagnostics based on the Gelman-Rubin criterion (Gelman & Rubin, 1992). To keep the number of free parameters in the halo model manageable, we a priori constrain the M_{0l} in equation 2.12 to the value of $\log M_{0l}/M_\odot = 11.5 \pm 1.7$ as determined by a fit to the low-redshift luminosity function at 250 μm (De Bernardis & Cooray, 2012) using data from Vaccari et al. (2010) and Dye et al. (2010). The best fit parameters and the uncertainties from the halo model fits are listed in Table 2.1.

2.6.1 Cirrus Amplitude and Cirrus Dust Temperature

We now discuss some of the results starting from our constraints on the cirrus fluctuations. The cirrus amplitudes have values of $(3.5 \pm 1.3) \times 10^5$, $(1.2 \pm 1.0) \times 10^4$ and $(1.1 \pm 0.9) \times 10^3$ Jy^2/sr at 250, 350 and 500 μm, respectively, at $\ell = 230$ corresponding to 100 arcminute

angular scales. These values are comparable to the cirrus amplitudes in the Lockman-Hole determined by Amblard et al. (2011). The GAMA-15 area we have used for this study is thus comparabale to some of the least Galactic cirrus contaminated fields on the sky. For comparison, the GAMA 9 hour area studied by Bracco et al. (2011) has cirrus amplitudes of $\sim 3 \times 10^7, 2 \times 10^6$ and 1×10^5 at 250, 350 and 500 μ, respectively. These are roughly a factor of 100 larger than the cirrus fluctuation amplitude in the GAMA-15 areas used here. The third field we considered for this study in GAMA 12 hour area was found to have cirrus amplitudes that are roughly a factor of 20 to 30 larger.

In order to determine if the cirrus dust in the GAMA-15 field is comparable to dust in the high cirrus intensity regions such as the GAMA-9 field, we fitted a modified blackbody model to the cirrus rms fluctuation amplitude. We found the dust temperature and the dust emissivity parameter β to be 21.1 ± 1.9 K and 2.9 ± 0.8, respectively. The results from the same analysis at 100 arcminute-scale rms fluctuations are 20.1 ± 0.9 and 1.3 ± 0.2 for dust temperature and emissivity, respectively. Even though the cirrus amplitude is lower with rms fluctuations, $\sqrt{C_i^{\rm cirrus}}$, at a factor of 10 below the GAMA-9 area studied in Bracco et al. (2011), we find the dust temperature to be comparable. It is unclear if the difference in the dust emissivity parameter is significant or captures any physical variations in the dust from high to low cirrus intensity, especially given the well-known degeneracy between dust temperature and β. Fluctuation measurements in all of the 600 sq. degree H-ATLAS fields should allow a measurement of β as a function of cirrus amplitude.

2.6.2 Faint Star-Forming Galaxy Statistics

Moving to the galaxy distribution, in Fig. **??**, we show the halo occupation distribution at $z = 1$ corresponding to the best-fit values of the parameters and the 1σ uncertainty region for three different luminosity cut-off values. At $z = 1$, as show in Fig. **??**, for $L_{\rm IR} > 10^9$

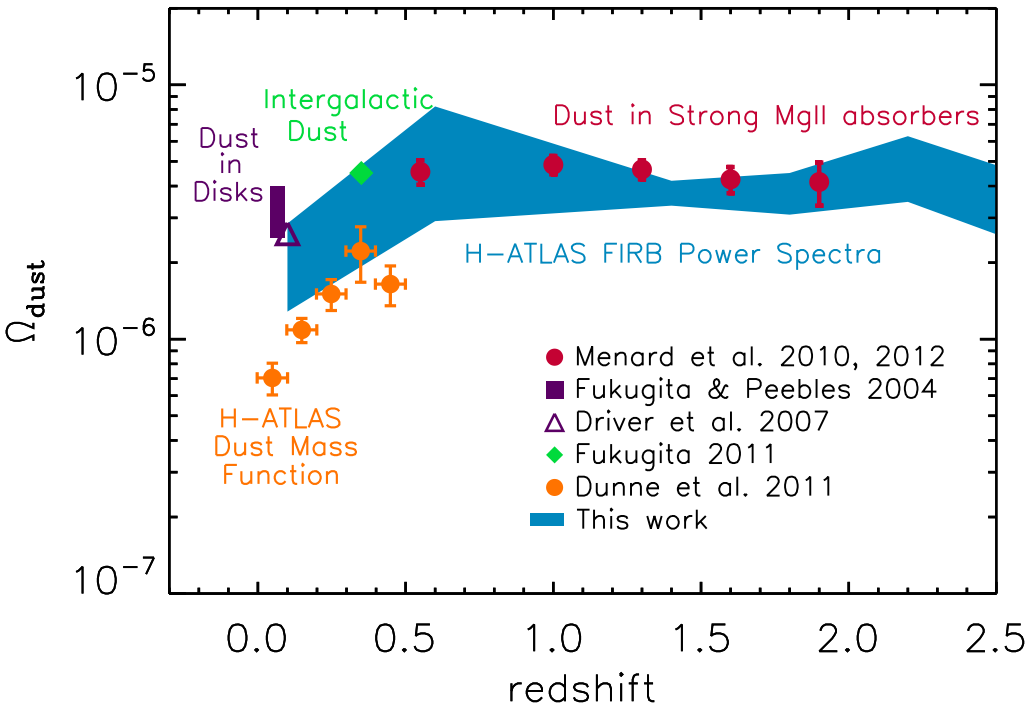

Figure 2.13: The cosmic density of dust Ω_{dust} vs redshift as determined from the CFIRB power spectra from H-ATLAS GAMA-15 field (shaded region). The thickness of the region corresponds to the $1-\sigma$ ranges of the halo model parameter uncertainties as determined by MCMC fits to the data (Table 1). We also compare our estimate to previous measurements in the literature. The measurements labeled H-ATLAS dust mass function are from the low-redshift dust mass function measurements in Dunne et al. (2011). The other estimates are based on extinction measurements from the SDSS (e.g., Ménard et al. 2010, 2012; Fukugita 2011; Fukugita & Peebles 2004) and 2dF (e.g., Driver et al. 2007).

$L_\odot$ galaxies, the HOD drops quickly for masses smaller than $\log(M_{\rm min}/M_\odot) \simeq 10.7$ and the high-mass end has a power-law behavior with a slope ~ 1. By design, this halo model based on CLFs has the advantage that it does not lead to unphysical situations with power-law slopes for the HOD greater than one as found by Amblard et al. (2011).

Both the HOD and the underlying luminosity-mass relations are consistent with De Bernardis & Cooray (2012), where a similar model was used to reinterpret Amblard et al. (2011) anisotropy measurement. The key difference between the work of De Bernardis & Cooray (2012) and the work here is that we introduce a dust SED to model-fit power spectra measurements in the three wavebands of SPIRE, while in earlier work only 250 μm measurements were used for the model fit. For comparison with recent model descriptions of the CFIRB power spectrum, we also calculate the effective halo mass scale given by

$$M_{\rm eff} = \int dM n_h(M) M \frac{N_T(M)}{n_g} \,. \tag{2.21}$$

With this definition we find $M_{\rm eff} = 3.2 \times 10^{12}$ $M_{\rm sun}$ at $z = 2$, consistent with the effective mass scales of Shang et al. (2011) and De Bernardis & Cooray (2012) of $M_{\rm eff} \sim 4 \times 10^{12}$ and slightly lower than the value of $\sim 5 \times 10^{12}$ from Xia et al. (2012).

The MCMC fits to the CFIRB power spectrum data show that the charicteristic mass scale M_{0l} evolves with redshift as $(1+z)^{-2.9\pm0.4}$. In order to compare this with existing models, we convert this evolution in the charachteristic mass scale to an evolution of the $L(M,z)$ relation. As $L(M) \propto (M/M_{0l})^{-\alpha_l}$, we find $L(M,z) \propto M_l^\alpha (1+z)^{-p_M \alpha_l}$. Using the best-fit values, we find $L(M,z) \propto M^{0.70\pm0.05}(1+z)^{2.0\pm0.4}$. In Lapi et al. (2011), their equation 9 with the SFR as a measure of the IR luminosity, this relation is expected to be $M(1+z)^{2.1}$. In Dekel et al. (2009), the expectation is $M^{1.15}(1+z)^{2.25}$. While we find a lower value for the power-law dependence on the halo mass with IR luminosity, the redshift evolution is consistent with both these models.

Note that in connecting SFR to IR luminosity we are simply using the modified black-body SED. The observational conversion from SFR to IR luminosity is calibrated over the range of 8 to 1000 μm. The modified black-body SED is likely only valid for 100 to 1000 μm for the region of the SED dominated by cold dust. Any hot dust, especially heated by AGNs, would not be accounted for. This probably results in an understimate of the SFR to IR luminosity conversion by about at most a factor of 2. However the exact correction should be relatively minor. Existing studies using templates show that the black-body thermal for cold dust is adequate for total IR luminosity for galaxies with $L_{\rm IR} < 10^{12}$ L$_\odot$, while the departure only exists for brightest galaxies with $L_{\rm IR} > 10^{12}$ L$_\odot$ where the AGN contribution is significant. Thus, for CFIRB power spectrum, it is unlikely that our results biasd by ignoring the presence of warm dust in our calculations and the parameters values derived under such an assumption. In future work we plan to address this issue further.

To test the overall consistency of our model relative to existing observations at the bright-end, in Fig. **??**, we compare the predicted luminosity functions 250 μm-selected galaxies in several redshift bins with existing measurements in the literature from Eales et al. (2010) and Lapi et al. (2011). The former relies on the spectroscopic redshifts in GOODS fields while the latter makes use of photometric redshifts. We find the overall agreement to be adequate given the uncertainties in the angular power spectrum and the resulting parameter uncertainties of the halo model. In future, the overall modeling could be improved with a joint-fit to both the angular power spectra and the measured luminosity functions.

In Fig. **??** we show the predicted redshift distributions of the 250 μm-selected galaxies in two 250-μm flux density bins in our model with a comparison to a measured redshift distribution with close to 900 optical spectra of Herschel-selected galaxies with Keck/LRIS and DEIMOS in Casey et al. (2012). While there is an overall agreement, for the brighter flux density bin, the measured redshift distribution shows a distinct tail a small, but non-negligible, fraction of galaxies at $z > 2$. It is unclear if those redshifts suggest the presence of bright galaxies

that are lacking in our halo model or if those redshifts are associated with lensed sub-mm galaxies (Negrello et al., 2010; Wardlow et al., 2012) with intrinstic fluxes that are below 10 mJy. If lensed, due to magnification boost, such fainter galaxies will appear in the brighter bin. We also note that the current halo model ignores any lensing effect in the anisotropy power spectrum. Existing models suggest that the lensing rate at 250 μm with flux densities below 50 mJy is small. At 500 μm, however, the lensed counts are at the level of 10% (Wardlow et al. 2012). While we do not have the signal-to-noise ratio for a lensing analysis of the far-IR background anisotropies with the current data and the power spectrum, a future goal of sub-mm anisotropy studies must involve characterizing the lensing modification to the power spectrum.

In Fig. **??** we show the redshift evolution of the emissivity predicted by our model at 250 μm according to equation 2.18. The shaded region shows the 1σ uncertainty associated with the best-fit model. For comparison we show the results of Viero et al. (2013); Valiante et al. (2009); Bethermin et al. (2011); Amblard et al. (2011); Gispert et al. (2000). The distribution predicted by our fit is consistent for a wide range of redshifts (up to $z > 3$) with Viero et al. (2013); Valiante et al. (2009); Bethermin et al. (2011); Amblard et al. (2011). The recent fit of Viero et al. (2013) to the HerMES angular power spectra shows a lower emissivity at both low-redshift ($z < 0.5$) and high-redshift ($z > 2.5$) ends.

The excess in the emissivity at the low-redshifts ($z < 0.1$) partly explains the difference in the power spectrum amplitude at 250 μm between the previous angular power spectra and H-ATLAS data. As discussed earlier, the GAMA-15 field of H-ATLAS is known to contain an overdensity of low-redshift galaxies. The brightest of these sources with $S_{250} > 50$ mJy are clearly visible in Fig. 2.2 when comparing the original and masked maps. While the $S_{250} > 50$ mJy mask is expected to remove a substantial fraction of the low-z population, we expect a fraction of the fainter ones to remain. Such galaxies are not present in the well-known extragalactic fields of the HerMES survey such as Lockman-Hole and the NDWFS-Bootes

field. The difference is a factor of ~ 2 amplitude increase in the power spectrum at 250 μm. As the excess population is primarily at low redshifts, the difference only shows up at 250 μm, while we do not see any significant difference at 350 and 500 μm between HerMES and H-ATLAS power spectra. The final result of this is to increase the emissivity at 250 μm at lowest redshifts $z < 0.1$ in our model relative to the emissivity function derived in Viero et al. (2013).

The H-ATLAS GAMA-15 field also shows an overall increase of bright counts at 250 μm relative to the HerMES fields (Rigby et al. in prep) and we verified that our suggestion of a factor of 2 increase in the power spectrum is coming from low-redshift galaxies is consistent with the differences in the number counts. The difference in the counts also explains the increase in the shot-noise at 250 μm relative to the value found in HerMES power spectra. These differences generally suggest that large field-to-field variations in the angular power spectrum with variations well above the typical Gaussian cosmic variance calculations. Such variations are readily visible when comparing individual field power spectra in Viero et al. (2013) (their Fig. 2.3).

Through our joint model-fit to 250, 350 and 500 μm power spectra, we also determine the SED of far-IR background anisotropies. To keep the number of free parameters in our model small, here we assume that the SED can be described by an isothermal black-body model. The best-fit dust temperature value that describes the far-IR fluctuations is 37 ± 2 K while the emissivity parameter β is unconstrained. In Fig. **??** we show the best-fit 68% and 95% confidence level intrvals of T_d and β, after marginalizing over all other parameters of the halo model. This figure makes it clear why we are not able to determine β with the current data due to degeneracies between the model parameters. The dust temperature we measure should be considered as the average dust temperature of all galaxies that is contributing to far-IR background anisotropy power spectrum. The dust temperature is higher than the typical 20K dust temperature derived from the absolute background spectra at far-IR

wavelengths from experiments such as FIRAS and Planck (Lagache et al., 2000).

This difference in the dust temperature could be understood since the absolute measurements, especially at degree angular-scale beams, are likely to be dominated by the Galactic cirrus, and thus the temperature measurement could be biased low. The dust temperature we measure from the far-IR power spectra is fully consistent with the the value of 44 ± 7K by Shang et al. (2011) in their modeling of the Planck far-IR power spectra (assuming the fixed value $\beta = 2$). Thus, while the best-fit SED model of the absolute CIB may suggest a low temperature value, the anisotropies from approximately 1-30 arcminute angular scales follow a SED with a higher dust temperature value. Separately, we also note that our dust temperature of 37 $\pm$2 K is also consistent with what Hwang et al. (2010) found in the GOODS-North field with *Herschel* andthe average dust temperature values of 36 ± 7 K (Chapman & Wardle, 2006; Dunne et al., 2000) for high-z SCUBA-selected sub-mm galaxies, but is somewhat higher than the average dust temperature value of 28 ± 8 K for Herschel-selected bright galaxies in Amblard et al. (2010). The Amblard et al. (2010) value is dominated by low-redshift ($z \sim 0.1$) galaxies with Herschel identifications to SDSS redshifts. In the local Universe, most dusty late-type galaxies show cold dust with temperatures around 20 K (Galametz et al., 2012; Davies et al., 2012). The higher temperature we find for the far-IR background anisotropies then suggests that the average interstellar radiation field in galaxies at $z \sim 1$ to 2 that dominate the dust emissivity is higher by a factor of 2^6 when compared that local late-type galaxies.

2.6.3 Cosmic Dust Abundance

The model described above allows us to estimate the fractional cosmic dust density:

$$\Omega_{\rm dust}(z) = \frac{1}{\rho_0} \int_{L_{min}} dL \phi(L, z) M_{dust}(L)\,, \tag{2.22}$$

where M_{dust} is the dust mass for a given IR luminosity and ρ_0 is the critical density of the Universe. Here we make use $\phi(L, z)$ as derived by the halo model fits to the far-IR background power spectra.

To convert luminosities to dust mass, we follow equation 4 in (Fu et al., 2012). This requires an assumption related to the dust mass absorption coefficient, κ_d. It is generally assumed that the opacity follows $\kappa_d(\nu) \propto \nu^\beta$ with a normalization of $\kappa_d = 0.07 \pm 0.02$ m^2 kg^{-1} at 850 μm (Dunne et al., 2000; James et al., 2002). This normalization, unfortunately, is highly uncertain and could easily vary by a factor of few or more (see discussion in James et al. 2002). The value we adopt here is appropriate for dusty galaxies and matches well with the integrated spectrum of the Milky Way.

The conversion to dust mass also requires the SED of dust emission. Here we make use of the average dust temperature value of 37 ± 2 K as determined by the model-fits to the angular power spectra. As β is undetermined from the data, we take its range with a prior between 1 and 2.5, consistent with typical values of 1.5 or 2 that is generally assumed in the literature. When calculating $\Omega_{\rm dust}(z)$ we marginalize over all parameter uncertainties so that we fully capture the full likelihood from the MCMC chains given the prior on β. Note that our assumption of a constant dust temperature is at odds with local late-type spirals that show much lower temperatures. However, it is also known that there are some sub-mm galaxies, especially those that are radio bright, with dust temperatures in the excess of 60 K. Thus with a value of 37 $\pm$2 K we may be using a representative average value for the dust temperature and an average of the dust SED for all galaxies at a variety of redshifts. Finally there are some indications that the dust temperature is IR luminosity dependent (see the discussion in Amblard et al. 2010). If that remains to be the case then the correct approch with eq. 2.22 will be to take into account that luminosity dependence as seen in the observations. Given that the current indications are coming from small galaxy samples, we do not pursue such a correction, but highlight that future studies could improve our dust

abundance estimate.

In Fig. 2.13 we show our results. In addition to the direct emission estimate that we have considered here, we also show the low-z dust abundances by integrating over the dust mass functions in Dunne et al. (2011). Those dust mass functions are limited to $z < 0.5$ due to the limited availability of spectroscopic data at higher redshifts. While in principle dust mass function captures the total dust of detected galaxies, the mass functions can be extrapolated to the faint-end, as has been done here, to acocunt for the fainter populations below individual detection levels. Thus the abundances from mass functions must agree with the estimates based on the anisiotropy measurements. We do not use our halo model to estimate the dust abundance at $z < 0.05$ since our halo model is normalized to the luminosity function of dusty galaxies at low redshifts.

Our measurement indicates that the dust density ranges between $\Omega_{\rm dust} \simeq 10^{-6}$ to 8×10^{-6} in the redshift range $z = 0.5 - 3$. We note that the $\Omega_{\rm dust}$ prediction of this work has a smaller uncertainty than that in De Bernardis & Cooray (2012) where the estimation was done assuming a larger range for T_d and β_d. In equation 2.22 we integrate over luminosities $L > 10^9$ $L_\odot$. However in this calculation the choice of minimum luminosity is less relevant, since the uncertainty on the dust density estimate is dominated by the large uncertainties of dust temperature and spectral emissivity index β.

Fig. 2.13 also summarizes the dust-density measurements of Fukugita & Peebles (2004); Driver et al. (2007); Menard et al. (2010); Fukugita et al. (2011). We have combined the points from Menard et al. (2010) for the dust contributions of halos and those from Menard & Fukugita, (2012) to a single set of data points, under the assumption that the amount of dust in halos doesn't evolve significantly with redshift. This is an assumption and could be tested in future data. At high redshifts our estimate is consistent with the results of Fukugita & Peebles (2004); Driver et al. (2007); Menard et al. (2010).

We note that the Ménard et al. (2010, 2012) measurements assume a reddening law appropriate for the SMC. A Milky Way reddening law would have resulted in a a factor of 1.8 higher dust masses, and thus dust abundance, than the values shown in Fig. 2.13 (see discussion in Ménard et al. 2012). Since the extinction measurements make use of a reddening law consistent with SMC while the direct emission measurements of the dust abundance that we show here assumed a dust mass absorption coefficient that is more consistent with the Milky Way, it is interesting to ask why the two measurements shown in Fig. 2.13 agree. The UV reddening law related to extinction based dust abundance estimates comes from small grains that dominate the absorption and scattering surface area. SMC differs from other galaxies in that it does not show a prominent 2200Å feature, which is assumed to come from carbon bonds (Pei, 1992). On the other hand, the far-IR emission that we have detected is likely dominated by large grains, usually assumed to be a mixture of silicates and carbonaceous grains. The difference in the reddening law between SMC and Milky Way then should not complicate the abundance estimates since extinction and emission may be coming from different populations of dust grains (e.g., Li & Draine (2002)).

While Fig. 2.13 is showing that the dust abundances from extinction measurements are consistent with direct emission measure from far-IR background fluctuations, the above discussion may suggest that this comparison is incomplete. It could be that this agreement is merely a concidence of two different populations. Thus the total abundance of the dust in the Universe is likely at most the total when summing up extinction and emission measurements. However, a direct summation of the two measurements is misleading and likely leads to an overestimate. While small and large grains dominate extinction and emission, respectively, the two effects are not exclusive in terms of the different populations of dust grains. Some of the grains associated with extinction must also be responsible for emission.

The far-IR background anisotropy measurements we have presented here have the advantage they capture the full population of grains responsible for thermal dust emission in galaxies.

The extinction measurements, however, are biased to clean lines of sights where the lines of sights do not cross the galactic disks. We have corrected for the missing dust in disks by adding the density of dust in disks at $z \sim 0.3$ to all measurements at high redshifts, but the disk dust density could easily evolve with redshift. The agreement we find here between the two different sets of measurements may, however, argue that there is no significant evolution in the dust density in galactic disks. In any case we suggest that one does not derive quick conclusions on the dust abundances or the agreements between extinction and emission measurements as shown in Fig. 2.13. There are built-in assumptions and biases between different sets of measurements and future studies must improve on the current analyses to understand the extent to which extinction and emission measurements can be used to obtain the total dust content of the universe.

While the *Herschel* fluctuation measurements have the advantage we see total emission, they have the disadvantage that we cannot separate the dust in disks to diffuse dust in halos that should also be emitting at far-IR wavelengths. In future, it may be possible to separate the two based on cross-correlation studies of far-IR fluctuations with galaxy catalogs and using stacking analysis, especially for galaxy populations at low redshifts. These are some of the studies that we aim to explore with the H-ATLAS maps in upcoming papers.

2.7 Conclusions

We have analyzed the anisotropies of the cosmic far-infrared background in the GAMA-15 Herschel-ATLAS field using the SPIRE data in the 250, 350 and 500 μm bands. The power spectra are found to be consistent with previous estimates, but with a higher amplitude of clustering at 250 μm. We find this increase in the amplitude and the associated increase in the shot-noise to be coming from an increase in the surface density of low-redshift galaxies that peak at 250 μm. The increase is also visible in terms of the bright source counts of the

Table 2.2: Angular power spectrum measurements at 250, 350 and 500 μm from GAMA-15 field of H-ATLAS. We tabulate the values as $l^2C_l/2\pi$ without shot-noise subtracted.

250 μm		350 μm		500 μm	
l	$l^2C_l/2\pi$ [Jy^2/Sr^2]	l	$l^2C_l/2\pi$ [Jy^2/Sr^2]	l	$l^2C_l/2\pi$ [Jy^2/Sr^2]
2.30×10^2	$(2.33 \pm 1.49) \times 10^{10}$	2.45×10^2	$(2.71 \pm 1.65) \times 10^9$	1.58×10^2	$(5.28 \pm 5.09) \times 10^8$
2.94×10^2	$(1.78 \pm 0.89) \times 10^{10}$	3.11×10^2	$(2.41 \pm 1.15) \times 10^9$	1.99×10^2	$(1.53 \pm 1.17) \times 10^8$
3.76×10^2	$(1.07 \pm 0.42) \times 10^{10}$	3.95×10^2	$(2.37 \pm 0.90) \times 10^9$	2.52×10^2	$(3.62 \pm 2.18) \times 10^8$
4.80×10^2	$(8.75 \pm 2.70) \times 10^9$	5.02×10^2	$(2.09 \pm 0.62) \times 10^9$	3.18×10^2	$(3.71 \pm 1.78) \times 10^8$
6.14×10^2	$(1.17 \pm 0.28) \times 10^{10}$	6.38×10^2	$(4.87 \pm 1.14) \times 10^9$	4.02×10^2	$(8.47 \pm 3.22) \times 10^8$
7.85×10^2	$(6.96 \pm 1.33) \times 10^9$	8.11×10^2	$(2.79 \pm 0.52) \times 10^9$	5.07×10^2	$(5.88 \pm 1.78) \times 10^8$
1.00×10^3	$(8.05 \pm 1.20) \times 10^9$	1.03×10^3	$(3.81 \pm 0.56) \times 10^9$	6.41×10^2	$(8.29 \pm 1.99) \times 10^8$
1.28×10^3	$(7.80 \pm 0.91) \times 10^9$	1.31×10^3	$(3.68 \pm 0.43) \times 10^9$	8.09×10^2	$(9.33 \pm 1.78) \times 10^8$
1.64×10^3	$(1.32 \pm 0.12) \times 10^{10}$	1.67×10^3	$(6.81 \pm 0.63) \times 10^9$	1.02×10^3	$(1.43 \pm 0.22) \times 10^9$
2.10×10^3	$(1.43 \pm 0.11) \times 10^{10}$	2.12×10^3	$(7.53 \pm 0.57) \times 10^9$	1.29×10^3	$(1.60 \pm 0.19) \times 10^9$
2.68×10^3	$(1.63 \pm 0.10) \times 10^{10}$	2.69×10^3	$(9.28 \pm 0.57) \times 10^9$	1.63×10^3	$(2.46 \pm 0.24) \times 10^9$
3.42×10^3	$(2.45 \pm 0.12) \times 10^{10}$	3.42×10^3	$(1.39 \pm 0.07) \times 10^{10}$	2.06×10^3	$(3.21 \pm 0.26) \times 10^9$
4.38×10^3	$(3.33 \pm 0.14) \times 10^{10}$	4.35×10^3	$(2.01 \pm 0.09) \times 10^{10}$	2.60×10^3	$(4.34 \pm 0.29) \times 10^9$
5.59×10^3	$(5.04 \pm 0.19) \times 10^{10}$	5.52×10^3	$(3.04 \pm 0.12) \times 10^{10}$	3.29×10^3	$(5.76 \pm 0.34) \times 10^9$
7.15×10^3	$(7.14 \pm 0.24) \times 10^{10}$	7.02×10^3	$(4.30 \pm 0.15) \times 10^{10}$	4.15×10^3	$(8.05 \pm 0.43) \times 10^9$
9.14×10^3	$(1.11 \pm 0.04) \times 10^{11}$	8.92×10^3	$(6.44 \pm 0.22) \times 10^{10}$	5.24×10^3	$(1.21 \pm 0.06) \times 10^{10}$
1.17×10^4	$(1.69 \pm 0.05) \times 10^{11}$	1.13×10^4	$(9.92 \pm 0.33) \times 10^{10}$	6.62×10^3	$(1.72 \pm 0.08) \times 10^{10}$
1.49×10^4	$(2.54 \pm 0.07) \times 10^{11}$	1.44×10^4	$(1.53 \pm 0.05) \times 10^{11}$	8.36×10^3	$(2.53 \pm 0.12) \times 10^{10}$
1.91×10^4	$(4.01 \pm 0.12) \times 10^{11}$	1.83×10^4	$(2.44 \pm 0.08) \times 10^{11}$	1.06×10^4	$(3.71 \pm 0.18) \times 10^{10}$
		2.33×10^4	$(3.92 \pm 0.12) \times 10^{11}$	1.33×10^4	$(5.79 \pm 0.29) \times 10^{10}$
				1.69×10^4	$(9.04 \pm 0.45) \times 10^{10}$
				2.13×10^4	$(1.55 \pm 0.07) \times 10^{11}$

H-ATLAS GAMA fields (e.g., Ribgy et al. in prep).

We have used a conditional luminosity function approach to model the anisotropy power spectrum of the far-infrared background. In order to fit H-ATLAS power spectra at the three wavebands of SPIRE we have adopted the spectral energy distribution of a modified black body and constrained the dust parameters T_d and β_d using a joint fit to power spectra at 250, 350 and 500 μm. The results of our fit substantially confirm previous results from the analysis of *Herschel* data and allow us to improve the constraints on the cosmic dust density that resides in the star forming galaxies responsible for the far-infrared background. We have found that the fraction of dust with respect to the total density of the Universe is $\Omega_{dust} = 10^{-6}$ to 8×10^{-6}, consistent with estimations from observations of reddening of metal-line absorbers.

Chapter 3

Cross-Correlation of Near and Far-Infrared Background Anisotropies as Traced by *Spitzer* and *Herschel*

3.1 Introduction

The cosmic infrared background (CIB) contains the total emission history of the Universe integrated along the line of sight. The CIB contains two peaks, one at optical/near-IR wavelengths around 1 μm and the second at far-IR wavelengths around 250 μm (Dole et al., 2006). The former is composed of photons produced during nucleosynthesis in stars while the latter is reprocessing of some of those photons by dust in the universe. While the total intensity in the near-IR background, especially at 3.6 μm, has been mostly resolved to individual galaxies, we are still far from directly resolving the total CIB intensity at 250 μm and above to individual sources. This is due to the fact that at far-IR wavelengths observations are strongly limited by the aperture sizes. With the SPIRE Instrument (Griffin et al., 2010)

aboard the *Herschel* Space Observatory (Pillbratt et al., 2010) [1], the background has been resolved to 5%, 15% and 22% at 250 μm, 350 μm and 500 μm, respectively (Oliver et al. , 2010). In order to understand some properties of the faint far-IR sources it is essential that we study the fluctuations or the anisotropies of the background.

These spatial fluctuations in the CIB are best studied using the angular power spectrum. This technique provides a way to study the faint and unresolved galaxies because while not individually detected, they trace the large scale structure. The clustering of these galaxies is then measurable through the angular power spectrum of the background intensity variations Amblard et al. (2011). Such fluctuation clustering measurements at far-IR wavelengths have been followed up with both *Herschel* and Planck (Viero et al., 2013; Planck Collaboration , 2014), the latter of which has provided the highest signal to noise calculation in the far-IR.

Separately near-IR background anisotropies have been studied in the literature and have been interpreted as due to galaxies containing PopIII stars present during reionization (Kashlinsky et al. , 2005, 2007, 2012), direct collapse black holes at $z > 12$ (Yue et al. , 2013), and intra-halo light (Cooray et al., 2012; Zemcov et al., 2014). In addition to *Spitzer* at 3.6 μm and above, fluctuation measurements in the near-IR wavelengths have come from Akari (Matsumoto et al. , 2011) and recently with the Cosmic Infrared Background Experiment (CIBER) at 1.1 and 1.6 μm (Zemcov et al., 2014). While earlier studies argued for a substantial contribution from galaxies at $z > 8$, including those with PopIII stars or blackholes, recent studies find that such signals are not likely to be the dominant contribution (Cooray et al., 2012; Yue et al. , 2014). Both Cooray et al. (2012) using *Spitzer* and Zemcov et al. (2014) using CIBER argue for the case that the signal is coming from low redshifts and proposes an origin that may be associated with intra-halo light. Intra-halo light invovles diffuse stars that are tidally stripped during galaxy mergers and other interactions. However, we still expect some signal from galaxies during reionization. In addition to these

[1]Herschel is an ESA space observatory with science instruments provided by European-led Principal Investigator consortia and with important participation from NASA.

two, there is also a third contribution. These are the faint, dwarf galaxies that are present between us and reionization. Such galaxies contribute to the near-IR and since they have flux densities below the point source detection level in near-IR maps, they remain unmasked during fluctuation power spectrum measurements. The exact relative amplitudes of each of these three signals are yet to be determined.

While fluctuations have been studied separately at far-IR and near-IR wavelengths, no attempt has been made to combine those measurements yet. In this work, we present the first results from just such a cross-correlation. We make use of the overlap coverage in the eight square degrees Boötes field between SDWFS at 3.6 μm (Ashby et al., 2009) and *Herschel* at 250, 350 and 500 microns. We find that the two signals are correlated but the cross-correlation coefficient is weak at 30% or below. Such a weak cross-correlation argues for the scenario that *Spitzer* and *Herschel* are mostly tracing two differerent populations. To interpret the data we model the auto and cross-correlation signals using a three component halo model composed of far infrared (FIR) galaxies, intra-halo light (IHL), and faint galaxies.

The paper is structured as follows. In Section 2, we discuss the data analysis and power spectra measurements. This includes the map making process for the *Herschel* and *Spitzer* data using HIPE and Self-Calibration, respectively. This section also explains the mask generation procedure, defines the cross-correlation power spectrum, and discusses sources of error. In Section 3, we describe the halo model including components for FIR galaxies, IHL, and faint galaxies and the MCMC process used to fit the data. Finally, in Sections 4 and 5 we present the results of our model fit, discuss the their implications, and give our concluding thoughts.

3.2 Data Analysis and Power Spectra Measurements

We discuss the analysis pipeline we implemented for the cross-correlation of *Herschel* and *Spitzer* fluctuations. The study is done in the Boötes field making use of the *Herschel*/SPIRE instrument data taken as part of the *Herschel* Multi-tiered Extragalactic Survey (HerMES; Oliver et al. 2012) and *Spizter*/IRAC imaging data taken as part of the *Spitzer* Deep Wide Field Survey (SDWFS) (Ashby et al., 2009). We describe the datasets, map-making, source masking and power spectrum measurement details in the sub-sections below.

3.2.1 Map Making

Far-IR maps with Herschel

We make use of the publicly available SPIRE instrument data of the Boötes field taken as part of HerMES from the ESA *Herschel* Science Data Archive [2]. Our map-making pipeline makes use of the Level 1 time-ordered scans that have been corrected for cosmic rays, temperature drifts, and bolometer time reponse as part of the standard data reduction by ESA. In those timelines we remove a baseline polynomial in a scan-by-scan basis to normalize gain variations. The SPIRE maps are generated using the *Herschel* Interactive Processing Environment (HIPE) (Ott, 2010). For this work we make use of the MADmap (Cantalupo et al., 2010) algorithm that is native to HIPE. It is a maximum likelihood estimate and follows the approach used in Thacker et al. (2013). We do not use the map-maker that was developed for anisotropy power spectrum measurement in (Amblard et al., 2010) due to improvements that have been made to the HIPE and its bulit-in map-makers since the Amblard et al. study in 2010.

The end products of the map-making process are single tile maps covering roughly 8 square

[2]Search with an AOR of "NDWFS/Bootes"

degrees and containing two sets of 80 scans in orthogonal directions with a pixel scale of 6 arcseconds per pixel in all SPIRE bands (250μm, 350μm, and 500μm). These maps, using publicly available data from HerMES, are generated at a pixel scale at a third of the beam size consisten with our previous work as well. Such a sampling allows the point source fluxes to be measured more accurately with an adequate sampling of the PSF. For this study, we are forced to compromise between an accurate sampling of the PSF, point source detection and flux density measurement to get an accurate combination of *Herschel* and *Spitzer* data. Since the native scale of *Spitzer* maps are at 1.2 arcseconds/pixel, we do not want to increase the SPIRE pixel scale substantially. We will return to this issue more below when we dicuss our point source masks that were applied to the maps to remove detected sources.

Spitzer

The SDWFS (Ashby et al., 2009) maps of the Boötes field consist of four observations taken over 7 to 10 days from 2004 to 2008[3]. For this analysis we limit our data to the 3.6μm channel. With four sets of data taken at different roll angles we can ensure our fluctuation measurements are robust to detector systematics. In addition, since the measurements were taken in different years and months, multiple jack-knife tests enable us to reduce and quantify the error from astrophysical systematics such as the zodiacal light (ZL).

To further control the errors and to obtain a uniform background measurement across a very wide area the maps are mosaiced using a Self-Calibration algorithm (Arendt et al., 2000). The algorithm is able to match the sky background levels with free gain parameters between adjacent overlapping frames using a least squares fitting technique. We make use of the cleaned basic calibrated data (cBCDs) publicly available from the *Spitzer* data archive for the map-making process. These frames have asteroid trails, hot pixels, and other artifacts

[3]http:sha.ipac.caltech.edu/applications/Spitzer/SHA/
Program number GO40839 (PI. D. Stern)

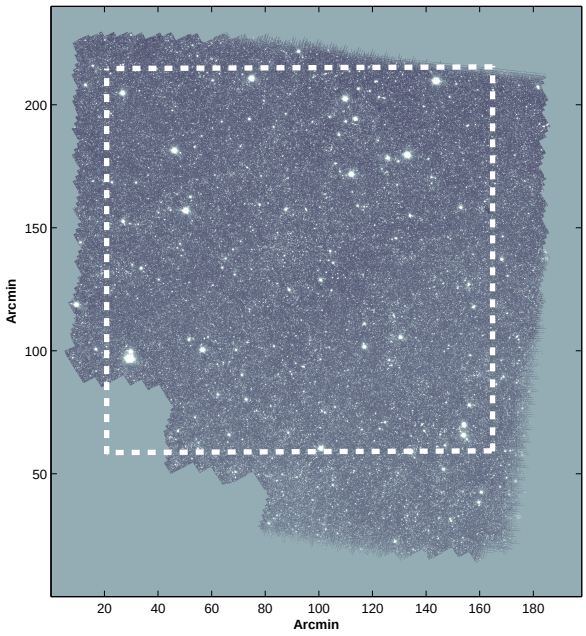

Figure 3.1: *Spitzer* 3.6μm Boötes field with only the overlapping area with *Herschel*. The white dashed lines show the cropped region used for the cross-correlation study. We crop to a rectangle to minimize the edge effects and biases from the non-uniform turn-around data in the *Herschel*/SPIRE scan pattern. This region is also selected to maximize the unmasked area.

removed. Our original maps are made at a pixel scale of 1.2 arcsecond per pixel. Unlike our previous work (Cooray et al., 2012), we have repixelized the maps to a 6 arcsecond per pixel scale to match with the pixel scale of our *Herschel* maps.

The *Spitzer* maps span an area of about 10 deg^2, larger than the *Herschel*/SPIRE coverage at 8 deg^2. For this study we extract the overlapping area in both *Spitzer* and *Herschel* as outlined in Figure 3.1.

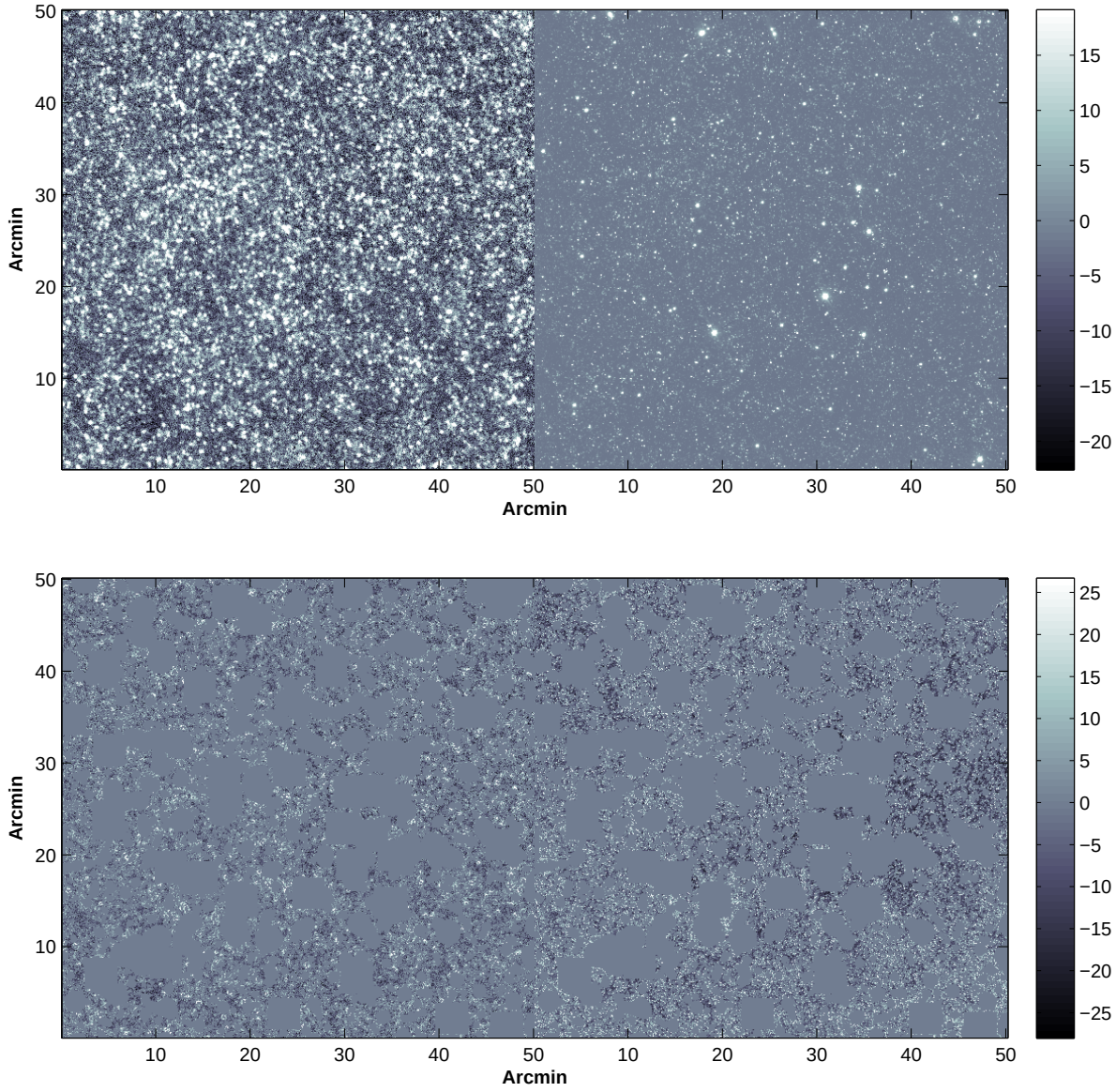

Figure 3.2: A zoomed in image, roughly 0.7 square degrees, of *Herschel* 250μm (left image) and *Spitzer* 3.6μm (right image) data of the Boötes/SDWFS field. The upper images are the unmasked maps showing all sources, while the lower images have the mask applied to remove bright detected sources from the cross-correlation study. The mask over the whole area removes 61.4% of the pixels leaving the remainder for the study presented here.

Astrometry

To ensure both *Herschel* and *Spitzer* images are registered to the same astrometric frame, we first checked for any offset in the *Spitzer* astrometry against the public catalog of SDWFS sources and corrected the astromerty using GAIA. We then made *Herschel* maps to the same astrometry as *Spitzer*. As a test on our overall astrometric calibration we used Source Extractor (SExtractor) (Bertin & Arnouts, 1996) to detect all sources in both the *Spitzer* and *Herschel* images. We then matched the sources in the two catalogs within a radius of 18 arcseconds (corresponding to the FWHM of the beam in 250μm). Next, we took these matches and subtracted their RA and DEC such that a perfect match would have a ΔRA and ΔDEC of zero. Fig. 3.3 shows a scatter plot of these values in pixels rather than RA and DEC. Perfectly aligned images would show a scatter centered at zero with equal spread in both directions. Our analysis shows a slight offset that is less than a pixel and within our tolerance as the effect on the cross-correlation is negligible since an offset less than a pixel will get binned to the nearest pixel and thus produces no offest.

3.2.2 Detected Source Masking

We remove the detected sources from our maps so the cross-correlation is aimed at the unresolved fluctuations in both sets of data. We first generate two masks, one for the *Spitzer* data and one for the *Herschel* data (in all three bands). We combine these two masks to a common mask. This guarantees that both sets of data are free of as much foreground contamination as possible, minimizing spurious correlations by having a masked area in one map that is unmasked in the other. With a common mask we are also able to better handle for mode-coupling effects which masking introduces. The final combined mask (a zoomed in portion can be seen in Fig. 3.2) removes 61.4% of the pixels.

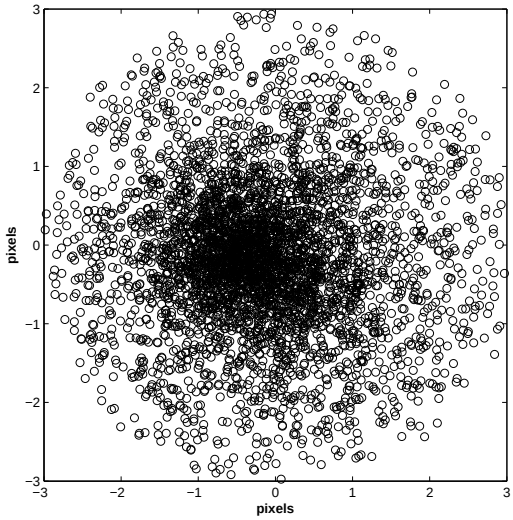

Figure 3.3: Using SExtractor on all of the maps (the example here shows pairs from 250μm and 3.6 μm) we generate a list of detected sources. All of the sources within a radius of 18 arcseconds of each map are identified to be counterparts of each other. For each counterpart we show the offset in their locations in *Herschel* and *Spitzer* maps where we have converted differences in RA and Dec to pixels. Plotted here is the ΔX and ΔY (in pixels) between 4252 sources selected from either *Herschel* or *Spitzer* with a detected counterpart in the other map.

Spitzer

Since our model is based on sources below the detection threshold, we must pay particular attention to generating a relatively deep mask for *Spitzer*. Otherwise unmasked *Spitzer* sources will correlate with the faint *Herschel* sources leading to a cross-correlation; in fact, as we find later, a significant fraction of the cross-correlation is due to faint *Spitzer* sources correlating with *Herschel* sources that are responsible for the SPIRE confusion noise.

We produce the *Spitzer* mask using a combination of catalogs from the NOAO Deep Wide Field Survey (NDWFS) in the B_w, R and I bands, and SExtractor) catalog that was generated for *Spitzer* maps at a 3-sigma detection threshold. As detailed in our previous work (Cooray et al., 2012), we start by iteratively running SExtractor with the same parameters used to generate the SDWFS catalogs (Ashby et al., 2009). This catalog is then combined with the NDWFS catalogs in the bands listed above. Like with the *Herschel* mask, we apply a flux cut, remove all pixels 5-sigma from the mean, and convolve everything with the PSF. Finally, we combine this mask with the *Herschel* mask.

Since this image has been rebinned to a larger pixel size by a factor of five at 6 arcsec from our previous work at 1.2 arcsec in Cooray et al. (2012), significant blending occurs from neary galaxies that are resolved in the 1.2 arcsec pixelized image. One effect of this is to increase the power at high-ℓ by increasing the shot-noise associated with unmasked galaxies. An aggressive mask for *Spitzer*, consistent with Cooray et al. (2012), cannot be used for this study since that will lead to a small fraction of unmasked pixels for the cross-correlation study with *Herschel*. Our main limitation here is not the depth of *Spitzer* imaging data, but the large PSF of *Herschel* maps. In Fig. 3.4 we compare the power specrum from Cooray et al. (2012) and the new power spectrum of *Spitzer* imaging data with a mask that retains more of the faint sources.

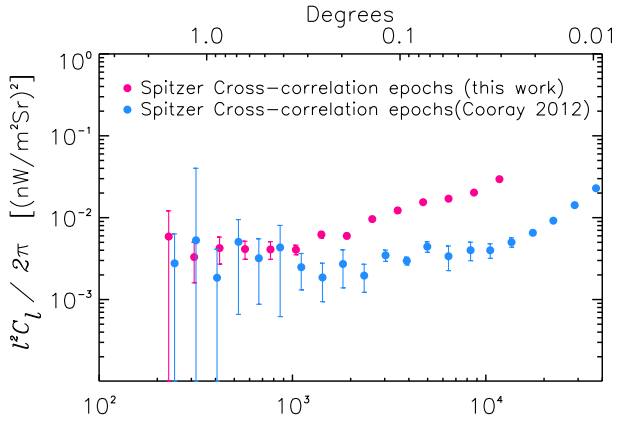

Figure 3.4: Comparison of *Spitzer* power spectra measured in the Boötes field between the current and previous work (Cooray et al., 2012). In the previous work the power spectra measured is the cross-correlation of epochs at 1.2 arcsec/pixel. In this work, however, we have repixilized the maps to 6 arcsec/pixel and created a new mask, which we are not able to make as deep, or else we would end up with no data.

Herschel

In the *Herschel* data, the mask is generated by a simple three step process in each of the SPIRE bands. They are then combined into a single mask. The zeroth step is to crop the region in which *Herschel* and *Spitzer* overlap into a rectangular area as shown in Fig. 3.1. First, we apply a flux cut at 50 mJy/beam, removing the brightest galaxies and staying consistent with our previous work on the clustering of fluctuations in the SPIRE bands (Amblard et al., 2011; Thacker et al., 2013). Next, to include the extended nature of the sources, we expand the mask by conlvolving with the point spread function (PSF). Finally, we remove pixels with no data, which arises mostly in 350 μm and 500 μm due to the enforced 6 arcsec pixel size (oversampling the PSF), and pixels with corrupt data by applying a 5-sigma clip to the images.

The final mask for this study is obtained by multiplying the individual *Herschel* and *Spitzer* masks for the union between the two maps. The auto power spectra we show in Fig. 3.5 use this combined mask between the two sets of data. A comparison of the shot-noise levels at

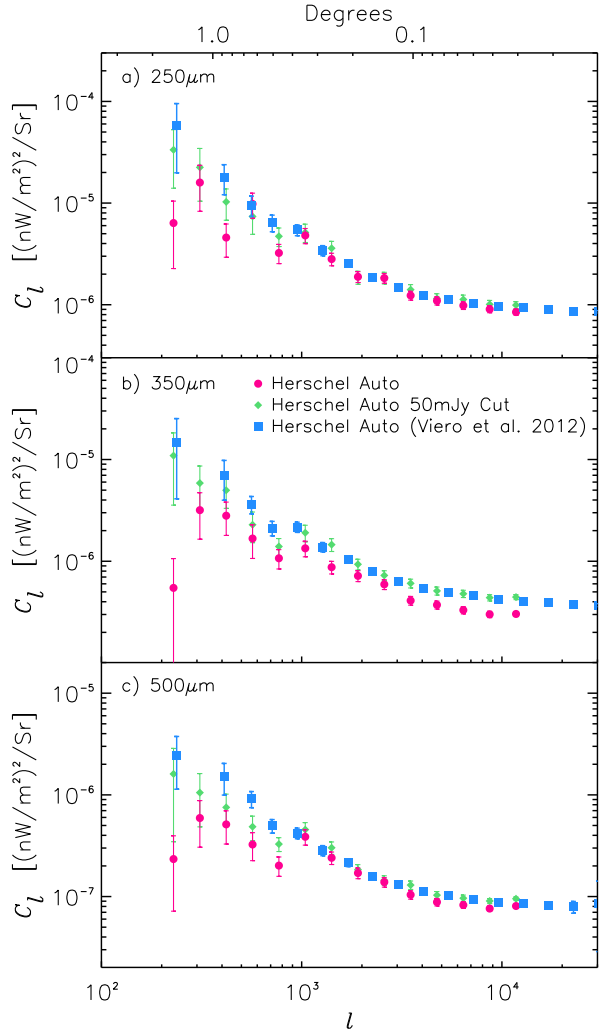

Figure 3.5: The comparison of *Herschel* auto-correlation power spectrum from our map (red points with a mask that removes 61.4% of the pixels) to the measurement in Viero et al. (2013) (blue points). The latter is based on a source mask that removes SPIRE sources brighter than 50 mJy. As discussed in Section 3.2.2 our effective flux density cut is at 29.5 mJy. In addition and just for comparison we also plot the auto-spectrum with a 50mJy/Beam flux cut in green.

high-ℓ for the *Herschel* power spectrum with models for source counts reveals that our final mask has an effective depth in the flux density cut at 250 μm of 29.5 mJy/beam. Fig. 3.5 shows the differences in the auto power spectra with our combined mask vs. power spectra measured with a mask based on a flux density cut for sources at 50 mJy.

3.2.3 Angular Power Spectra and Sources of Error

Our power spectra and cross power spectra measurements follow the procedures we have used for past work (Thacker et al., 2013; Cooray et al., 2012). Here we summarize the key ingredients related to the uncertainties of the power spectrum measurements.

Instrumental Noise

One benefit of a cross-correlation is that instrumental noise is minimized, especially between two different detectors or imaging experiments. The maps can be thought of as signal, S, plus a noise component, N. So in a cross-correlation we have $M_1 \times M_2 = (S_1 + N_1) \times (S_2 + N_2)$. Since the noise is expected to be random and because these are two different detectors, the noise should be uncorrelated, thus dropping out of the cross-correlation.

To get a handle on the instrumental noise component and an estimate of systematic errors like zodiacal light or cirrus contamination, we perform jacknife tests. These tests involve taking half maps for *Herschel* and single epoch maps for *Spitzer* and cross-correlating their differences. For example in *Spitzer* we would take epochs $(1-2)$ cross correlated with epochs $(3-4)$, where 1 to 4 are the four epochs of the SWDFS survey. We average all combinations of this and find it is is stationary about zero. Finally, the variance arising from this is an estimate of the residual noise and is added to the total error budget of the *Spitzer* auto power spectrum.

While it is assumed that the detector noise components of *Herschel* and *Spitzer* do not correlate, we still need to place a limit on any residual noise correlations in the cross-correlation. This is accomplished by taking null tests where we cross-correlate a *Herschel* map with all combinations of epoch differenced maps of *Spitzer*. The variance of this multi epoch cross-correlations are added to our error budget of the *Herschel* and *Spitzer* cross-correlation power spectrum.

Beam Correction

At high ℓ there is a substantial drop in power due to the finite resolution of the detector and this drop in power needs to be accounted for. This is corrected by taking the power spectrum of the PSF (point spread function) and normalizing to be one at low ℓ. For cross spectra we need a correction for the two separate beams. For that we simply use the geometric mean of the two beams. For the *Herschel* data we use the beam calculated by Amblard et al. (2011) based on observations of Neptune. The *Spitzer* beam used was calculated in Cooray et al. (2012) directly from the PSF as described there.

Mode-Coupling Correction

Unlike the case of CMB, infrared background power spectra involves aggressive masks that remove a substantial fraction of the pixels. A consequence of such masking is breaking up larger Fourier modes into smaller modes. This results in a shift of power from low-ℓ to high-ℓ. Using the method from Cooray et al. (2012) we generate a mode-coupling matrix, $M_{\ell\ell'}$, shown in Fig. 3.6 by making maps of pure tones, masking them, and taking the power spectrum. Thus, by construction the matrix transforms unmasked power to masked power and we simply invert the matrix to obtain a transormation to an unbiased power spectrum.

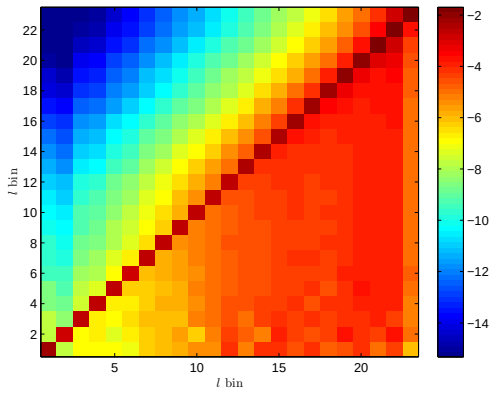

Figure 3.6: Mode-coupling matrix $M_{ll'}$ for the combined mask (log scale).

Map Making Transfer Function

Unfortunately the map making process does not result in a perfect representation of the sky. The map making process can induce ficticious correlations or suppress them based on deficiencies in the scan pattern, the technique that was used to process the timeline data including any filtering that was applied. We capture all of the modifications associated with the map making process by the transfer function, $T(l)$.

For *Herschel* data we calculate the transfer function by making 100 Gaussian random maps and reading them into timeline data using the same pointing information as the actual data. Then we produce artificial maps from these timelines and take the average of the power spectra of each of these maps to the power spectrum in each of the input maps. For the *Spitzer* data, we follow a similar approach but instead of reading data into timelines we create small tiles that are re-mosaiced using the same self-calibration algorithm as the actual data. These simulated tiles include Gaussian fluctuations and instrumental noise consistent with the corresponding tile in the actual data. Due to the dithering and tiling pattern that was used for actual observations in SDWFS with *Spitzer*, the map-making transfer function is essentially one at all angular scales of interest. This is substantially different for *Herschel*/SPIRE with a transfer function that departs from one at low and high ℓ as shown

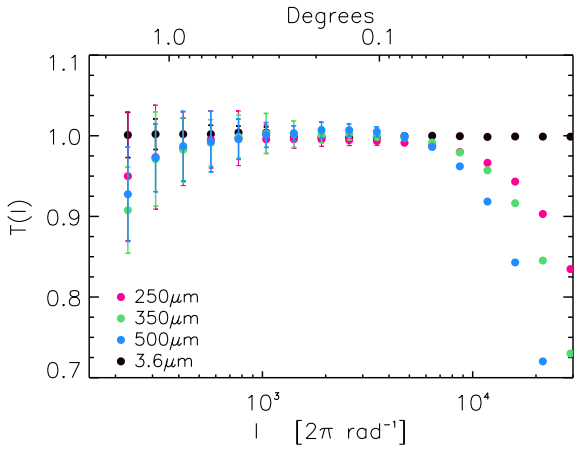

Figure 3.7: Map-making transfer function $T(l)$ for the *Herschel* and *Spitzer* Boötes field anisotropy power spectrum. The uncertainties in the transfer function are calculated from 100 gaussian realizations of the sky as described in Section 3.2.3.

in Fig. 3.7. The difference at high ℓ is due to the scan pattern that leaves stripes in the data; the difference at low ℓ or large angular scales is due to the filtering that was applied to timeline data to remove gain drifts during an individual scan. That is the process used to make maps and to ensure the map-making process has not generated a bias in the power spectrum.

Power Spectrum Estimate

To put these corrections to use, we must first define the cross-correlation. Given two maps H and S, the cross-correlation is calculated as:

$$\langle C_{l_i} \rangle = \frac{\sum_{l_1}^{l_2} w(l_x, l_y) \widetilde{H}(l_x, l_y) \widetilde{S}^*(l_x, l_y)}{\sum_{l_1}^{l_2} w(l_x, l_y)}, \tag{3.1}$$

where $\widetilde{H}$ and $\widetilde{S}$ are the 2D Fourier transforms of their respective maps and $w(l_x, l_y)$ is the mask in Fourier space. The auto-spectra follows the case when $H = S$.

Finally, the final cross power spectrum estimate is obtained from the measured power spectrum, $\widetilde{C_{\ell'}}$, with above described corrections as:

$$C_\ell = \frac{M^{-1}_{\ell\ell'}\widetilde{C_{\ell'}}}{T_{\ell'} b^S_{\ell'} b^H_{\ell'}} \,. \tag{3.2}$$

To generate the Spitzer auto-spectrum (Fig 3.4) we take the average of the permuations of different cross-correlations involving the four epochs of SDWFS. For example, we calculate $(1+2)\times(3+4)$ averaged with all other permuatations where 1 to 4 are the four epochs. When compared to our previous work Spitzer auto-spectrum deviates at high ℓ. The higher shot-noise is because we have repixelized the image from 1.2 arcsec/pixel in our prior work to 6 arcsec/pixel here. This also leads to a more shallow mask than our previous work.

Figure 3.8 shows the cross-correlations with the best-fit model (described below) shown for comparison. Again, we make use of the four different *Spitzer* epochs in the cross-correlation. The cross-correlation is calculated as the average of $(\mathrm{epoch}_i + \mathrm{epoch}_j)/2 \times$ *Herschel* where $i \neq j$.

In addition to the instrumental noise term and errors coming from the uncertainities in the beam function and map-making transfer function, we also account for the cosmic variance in our total error budget. More details are available in the Appendix A.3.

3.3 Halo Model

In this Section, we outline our model for the cross-correlation. The underlying model involves three key components: far-IR galaxies, intra-halo light, and near-IR galaxies.

3.3.1 Model for FIR background fluctuations from star-forming dusty galaxies

We make use of the conditional luminosity function (CLF) models to calculate the power spectrum of FIR galaxies (Lee et al. , 2009; De Bernardis & Cooray, 2012). The probability density of a halo/subhalo with mass M to host a galaxy observed in a FIR band with luminosity L (i.e. L_{250}, L_{350} and L_{500} in this work) is given by

$$P(L|M) = \frac{1}{\sqrt{2\pi}\ln(10)L\Sigma}\exp\left\{-\frac{\log_{10}[L/\bar{L}(M,z)]^2}{2\Sigma^2}\right\}, \tag{3.3}$$

where $\Sigma = 0.3$ Lee et al. (2009) is the variance of $\log_{10}\bar{L}(M,z)$, and $\bar{L}(M,z)$ is the mean luminosity given a halo/subhalo mass M at redshift z which takes the form

$$\bar{L}(M,z) = \bar{L}(M)(1+z)^p F_\nu[\nu_{\rm obs}(1+z)], \tag{3.4}$$

where we have

$$\bar{L}(M) = L_0\left(\frac{M}{M_0}\right)^\alpha \exp\left[-\left(\frac{M}{M_0}\right)^\beta\right]. \tag{3.5}$$

Here we take $M_0 = 10^{12}\ M_\odot$ consistent with previous work (Lee et al. , 2009; Cooray et al., 2012), L_0, α and β as free parameters to be fitted by the data [4]. We also consider the redshift evolution of $\bar{L}(M)$ with a factor $(1+z)^p$, where p is a free parameter. The F_ν is spectral energy distribution (SED) for FIR galaxies, which takes into account the fact that the observed frequency $\nu_{\rm obs}$ comes from the frequency $\nu = \nu_{\rm obs}(1+z)$ at z. The SED can be expressed in terms of a modified blackbody normalized at 250 μm

$$F_\nu = \frac{(1-e^{-\tau})B(\nu,T_d)}{(1-e^{-\tau_0})B(\nu_0,T_d)}, \tag{3.6}$$

[4]We set $\beta = 0$ when we perform the fitting process since we find β is close to zero as a free parameter (De Bernardis & Cooray, 2012).

where $B(\nu, T_d)$ is the blackbody spectrum, T_d is the dust temperature of FIR galaxies, ν_0 is the frequency of 250 μm, $\tau = (\nu/\nu_0)^{\beta_d}$, $\tau_0 = \tau(\nu_0)$ and β_d is the dust emissivity spectral index. We fix $T_d = 35$ K and $\beta_d = 2$ in this work which are consistent with results from observations (Shang et al., 2011; Hwang et al., 2010; Chapman & Wardle, 2006; Dunne et al., 2000; Amblard et al., 2010).

Then the luminosity function (LF) can be obtained by

$$\Phi(L, z)dL = dL \int dM P(L|M) n(M, z), \tag{3.7}$$

where $n(M, z) = n_h(M, z) + n_s(M, z)$ is the total halo mass function, and n_h and n_s are halo and subhalo mass function respectively. In this work, we find that subhalos are not important and cannot affect our results, so we ignore all subhalo terms in our analysis for simplicity, and we have $n(M, z) \simeq n_h(M, z)$. Next, we can estimate the mean comoving emissivity of FIR galaxies, $\bar{j}_\nu(z)$, at frequency ν and redshift z

$$\bar{j}_\nu(z) = \frac{1}{4\pi} \int \Phi(L, z) L dL. \tag{3.8}$$

Also, we can construct the halo occupation distribution (HOD) with the probability density shown by equation (3.3). Given a luminosity limit $L_{\rm min}$ determined by a survey,the average number of central galaxies hosted by halos of mass M is

$$\langle N_c(M) \rangle_{L \geq L_{\rm min}} = \int_{L_{\rm min}} P(L|M) dL. \tag{3.9}$$

The 1-halo and 2-halo terms of 3-D power spectrum for FIR galaxies are given by

$$P_{\rm gg}^{\rm 1h}(k,z) = \int dM n(M,z) \frac{\langle N_{\rm g}(N_{\rm g}-1)\rangle}{\bar{n}_{\rm g}^2} u^p(k|M,z), \tag{3.10}$$

$$P_{\rm gg}^{\rm 2h}(k,z) = \left[\int dM b(M,z) n(M,z) \frac{\langle N_{\rm g}\rangle}{\bar{n}_{\rm g}} u(k|M,z)\right]^2 \times P_{\rm lin}(k,z), \tag{3.11}$$

where $u(k|M,z)$ is the Fourier transform of the Navarro-Frenk-White (NFW) halo density profile for halos of mass M at redshift z (Navarro et al., 1997), and the power index p takes $p=1$ when $\langle N_{\rm g}(N_{\rm g}-1)\rangle \leq 1$ and $p=2$ otherwise (Cooray & Sheth, 2002). $b(M,z)$ is the halo bias (Sheth & Tormen, 1999), and $P_{\rm lin}$ is the linear matter power spectrum. The $\bar{n}_{\rm g}$ is the galaxy mean number density which is expressed as

$$\bar{n}_{\rm g}(z) = \int dM n(M,z) \langle N_{\rm g}(M)\rangle. \tag{3.12}$$

Here $\langle N_{\rm g}(M)\rangle$ is the mean number of galaxies hosted by a halo of mass M. Since we ignore the subhalo term in this work, we assume $\langle N_{\rm g}(M)\rangle \simeq \langle N_c(M)\rangle$ and $\langle N_{\rm g}(N_{\rm g}-1)\rangle \simeq \langle N_c(M)\rangle^2$, which is a good approximation in our calculation.

The 2-D angular cross-power spectrum of FIR galaxies at observed frequencies ν and ν' can be obtained with the help of Limber approximation as

$$C_{\ell,{\rm FIR}}^{\nu\nu'} = \int dz \left(\frac{d\chi}{dz}\right)\left(\frac{a}{\chi}\right)^2 \bar{j}_\nu(z)\bar{j}_{\nu'}(z) P_{\rm gg}(k,z), \tag{3.13}$$

where χ is the comoving distance, a is the scale factor, $\bar{j}_\nu(z)$ is the mean emissivity shown in equation (3.8), and $P_{\rm gg}(k,z) = P_{\rm gg}^{\rm 1h}(k,z) + P_{\rm gg}^{\rm 2h}(k,z)$ is the galaxy power spectrum where $k = \ell/\chi$.

3.3.2 Intra-Halo Light

According to Cooray et al. (2012), intra-halo light (IHL) mean luminosity for halos with mass M at redshift z is assumed to be

$$\bar{L}_{\rm IHL}(M,z) = f_{\rm IHL}(M) L^{2.2}(M)(1+z)^{p_{\rm IHL}} F_\lambda^{\rm IHL}, \tag{3.14}$$

where $f_{\rm IHL}(M)$ is the IHL fraction of the total halo luminosity, which has the form

$$f_{\rm IHL}(M) = A_{\rm IHL}\left(\frac{M}{M_0}\right)^{\alpha_{\rm IHL}}. \tag{3.15}$$

Here $A_{\rm IHL}$ is an amplitude factor and $\alpha_{\rm IHL}$ is a mass power index fixed to be 0.1 (Cooray et al., 2012). $L^{2.2}(M) = L_0^{2.2}(M)/\lambda_0$ is the total halo luminosity at 2.2 μm, where $\lambda_0 = 2.2$ μm and $L_0^{2.2}(M)$ is given by (Lin et al., , 2004)

$$L_0^{2.2}(M) = 5.64\times10^{12} h_{70}^{-2}\left(\frac{M}{2.7\times10^{14} h_{70}^{-1} M_\odot}\right)^{0.72} L_\odot. \tag{3.16}$$

Then we can scale the total luminosity at 2.2 μm to the other wavelengths by the IHL SED $F_\lambda^{\rm IHL}$. Here the IHL SED is assumed to be the SED of old elliptical galaxies which are composed of old and red stars (Krick & Bernstein, 2007), and we normalize $F_\lambda^{\rm IHL} = 1$ at 2.2 μm.

The 1-halo and 2-halo terms of the 2-D IHL angular cross-power spectrum at observed

wavelengths λ and λ' can be estimated by

$$
\begin{aligned}
C_{\ell,\mathrm{IHL}}^{\lambda\lambda',1\mathrm{h}} &= \frac{1}{(4\pi)^2}\int dz \left(\frac{d\chi}{dz}\right)\left(\frac{a}{\chi}\right)^2 \\
&\quad \times \int dM n(M,z) u^2(k|M,z) \bar{L}_{\mathrm{IHL}}^{\lambda} \bar{L}_{\mathrm{IHL}}^{\lambda'}, \qquad (3.17) \\
C_{\ell,\mathrm{IHL}}^{\lambda\lambda',2\mathrm{h}} &= \frac{1}{(4\pi)^2}\int dz \left(\frac{d\chi}{dz}\right)\left(\frac{a}{\chi}\right)^2 P_{\mathrm{lin}}(k,z) \\
&\quad \times \int dM b(M,z) n(M,z) u(k|M,z) \bar{L}_{\mathrm{IHL}}^{\lambda} \\
&\quad \times \int dM b(M,z) n(M,z) u(k|M,z) \bar{L}_{\mathrm{IHL}}^{\lambda'}. \qquad (3.18)
\end{aligned}
$$

The total 2-D IHL angular cross-power spectrum is then given by

$$
C_{\ell,\mathrm{IHL}}^{\lambda\lambda'} = C_{\ell,\mathrm{IHL}}^{\lambda\lambda',1\mathrm{h}} + C_{\ell,\mathrm{IHL}}^{\lambda\lambda',2\mathrm{h}}. \qquad (3.19)
$$

3.3.3 Model for NIR background fluctuations from known galaxy populations

We follow Helgason et al. (2012) to estimate the NIR background fluctuations from known galaxy populations. We make use of their empirical fitting formulae of luminosity functions (LFs) for measured galaxies in UV, optical and NIR bands out to $z \sim 5$. Then, we estimate the mean emissivity $\bar{j}_\nu(z)$ at the rest-frame frequencies and redshift to the observed frequency. We adopt the HOD model to calculate the 3-D galaxy power spectrum using equation (3.10) and (3.11) with $\langle N_{\mathrm{g}}\rangle = \langle N_c\rangle + \langle N_s\rangle$ and $\langle N_{\mathrm{g}}(N_{\mathrm{g}}-1)\rangle \simeq 2\langle N_s\rangle\langle N_c\rangle + \langle N_s\rangle^2$, where

$$
\langle N_c\rangle = \frac{1}{2}\left[1 + \mathrm{erf}\left(\frac{\log_{10}M - \log_{10}M_{\mathrm{min}}}{\sigma_M}\right)\right], \qquad (3.20)
$$

and

$$\langle N_s \rangle = \frac{1}{2}\left[1 + \mathrm{erf}\left(\frac{\log_{10}M - \log_{10}2M_{\rm min}}{\sigma_M}\right)\right]\left(\frac{M}{M_s}\right)^{\alpha_s}. \tag{3.21}$$

Here $M_{\rm min}$ denotes the mass that a halo has 50% probability of hosting a central galaxy, and σ_M is the transition width. We assume the satellite term has a cutoff mass with twice the mass of central galaxy and grows as a power law with slope α_s and normalized by M_s. We set $M_{\rm min} = 10^9\ M_\odot$, $\sigma_M = 0.2$, $M_s = 5 \times 10^{10}\ M_\odot$, and $\alpha_s = 1$ (Helgason et al., 2012). The 2-D angular cross-power spectrum $C_{\ell,\rm NIR}^{\nu\nu'}$ can be calculated by equation (3.13) with $\bar{j}_\nu(z)$ and $P_{\rm gg}(k,z)$ of unresolved galaxies.

3.3.4 Model Comparison

In this work, we have three angular auto power spectra $C_\ell^{\rm Her}$ in the far-infrared from *Herschel*/SPIRE at 250, 350 and 500 μm, one angular auto power spectrum $C_\ell^{\rm Spi}$ from *Spitzer* at 3.6 μm, and three cross-power spectra $C_\ell^{\rm cross}$ between *Herschel* and *Spitzer* data. Using the models discussed in the previous Sections, we fit all these auto and cross power spectra with a single model.

As mentioned, we consider three components in our model to fit each dataset. For $C_\ell^{\rm Her}$, we have $C_\ell^{\rm Her} = C_\ell^{\rm FIR} + C_{\ell,\rm shot}^{\rm Her}$, where $C_\ell^{\rm FIR} = C_{\ell,\rm FIR}^{\nu\nu'}$, $\nu_{\rm obs}, \nu'_{\rm obs}$ are the observed frequencies at 250, 350 or 500 μm, and $C_{\ell,\rm shot}^{\rm Her}$ is the shot-noise term. In a similar way, for $C_\ell^{\rm Spi}$, we take $C_\ell^{\rm Spi} = C_\ell^{\rm NIR} + C_\ell^{\rm IHL} + C_{\ell,\rm shot}^{\rm Spi}$ at 3.6 μm. For $C_\ell^{\rm cross}$, it is expressed as $C_\ell^{\rm cross} = C_\ell^{\rm FIR\times NIR} + C_\ell^{\rm FIR\times IHL}$. The model details of these cross powerspectra are outlined in the Appendix.

Since the shot-noise is a constant and dominant at high ℓ, we derive the shot-noise terms from the data at the high ℓ and fix them in the fitting process. The values of the shot-noise terms we find are $C_{\ell,\rm shot}^{\rm Her} = 8.4 \times 10^{-7}, 3.0 \times 10^{-7}$ and 8.0×10^{-8} nW^{2}m^{-4}sr^{-1}, and $C_{\ell,\rm shot}^{\rm cross} =$

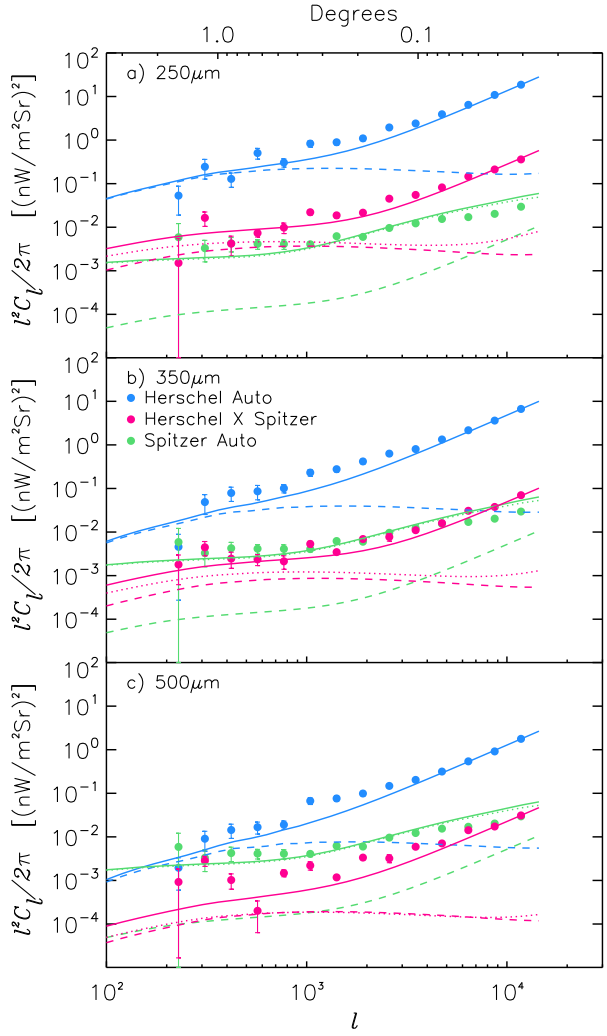

Figure 3.8: The auto and cross angular power spectra of Herschel (at 250, 350 and 500 μm) and *Spitzer* (at 3.6 μm) surveys. The blue solid and dashed lines are the total fitting results and FIR galaxy power spectra, respectively. The green solid, dotted, and dashed are the fittings for the total, IHL and NIR galaxy power spectra. The pink solid line is the total cross-power spectrum fit while the dotted and dashed correspond to far-IR cross IHL and far-IR cross near-IR respectively.

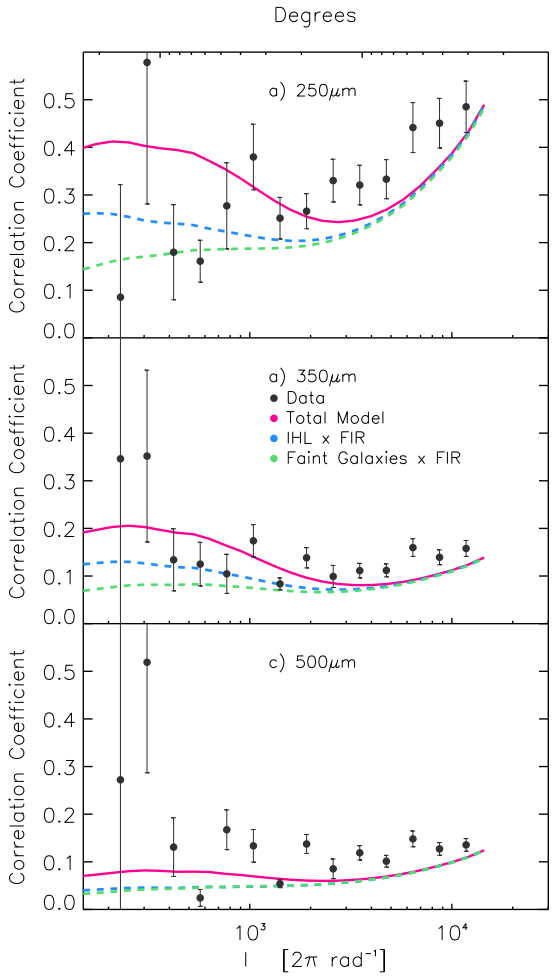

Figure 3.9: Correlation coefficient for the cross-correlation of Herschel and *Spitzer* (250, 350, 500 μm $\times$ 3.6 μm). The pink line corresponds to the total best fit halo model. The blue and green dashed lines show the component breakdown of the total halo model into the two terms that make up the total cross correlation. The blue line results from the correlation between IHL and FIR while the green line is from faint galaxies in the NIR correlated with FIR.

$1.7 \times 10^{-8}, 3.0 \times 10^{-9}$ and 1.4×10^{-9} nW^{2}m^{-4}sr^{-1} at 250, 350 and 500 μm, respectively. For $C_{\ell,\rm shot}^{\rm Spi}$, we scale the shot-noise of NIR background $C_{\ell,\rm shot}^{\rm NIR}$ given by equation (13) in Helgason et al. (2012) to match the high-ℓ data of *Spitzer* at 3.6 μm. This is done by adjust the minimum apparent magnitude $m_{\rm min}$, and we find $m_{\rm min} = 23$ which gives $C_{\ell,\rm shot}^{\rm NIR} = 3.1 \times 10^{-10}$ nW^{2}m^{-4}sr^{-1}.

We employ the Markov Chain Monte Carlo (MCMC) method to perform the fitting process. The Metropolis-Hastings algorithm is adopted to determine the probability of accepting a new MCMC chain point (Metropolis et al., 1953). We use χ^2 distribution to calculate the likelihood function $\mathcal{L} \propto \exp(-\chi^2_{\rm tot}/2)$. For the three datasets, we have $\chi^2_{\rm tot} = \chi^2_{\rm Her} + \chi^2_{\rm Spi} + \chi^2_{\rm cross}$, and the χ^2 is given by

$$\chi^2 = \sum_{i=1}^{N_{\rm d}} \frac{(C_\ell^{\rm obs} - C_\ell^{\rm th})^2}{\sigma_\ell^2}, \tag{3.22}$$

where $N_{\rm d}$ is the number of the data points, $C_\ell^{\rm obs}$ and $C_\ell^{\rm th}$ are the angular power spectra from observation and theory, and σ_ℓ is the error for each data point.

For simplicity we take $z_{\rm min} = 0$, $z_{\rm max} = 6$, $M_{\rm min} = 10^9\ h^{-1}M_\odot$ and $M_{\rm max} = 10^{14}\ h^{-1}M_\odot$ when we calculate the integral over redshift and halo mass in the power spectra. We use a uniform prior probability distribution for the free parameters in our model. The parameters and their ranges are as follow: $\log_{10}L_0 \in (-9, 1)$, $\alpha \in (-5, 5)$, $p \in (0, 5)$ for the FIR galaxy model, and $A_{\rm IHL} \in (-5, 0)$, $p_{\rm IHL} \in (-5, 5)$ for the IHL model. We generate twelve parallel MCMC chains for each dataset, and collect about $120,000$ chain points after the chains reach convergence. After the burn-in process and thinning the chains, we merge all the chains together and get about $10,000$ chain points to illustrate the probability distribution of the free parameters. The details of our MCMC method can be found in Gong & Chen (2007).

Table 3.1: The best-fit values and 1σ errors of the model parameters from the MCMC constraints.

	250 μm	350 μm	500 μm
$\log_{10} L_0$	-6.5 ± 0.5	-7.0 ± 0.5	-7.9 ± 1.1
α	0.23 ± 0.06	0.24 ± 0.08	0.22 ± 0.11
p	3.9 ± 0.12	3.9 ± 0.20	3.9 ± 0.25
$\log_{10} A_{\rm IHL}$	-1.70 ± 0.04	-1.75 ± 0.04	-1.74 ± 0.04
$p_{\rm IHL}$	-3.2 ± 0.4	-2.5 ± 0.3	-2.6 ± 0.3

3.4 Results and Discussion

In this Section, we discuss the results from the data analysis and the MCMC model fits to the auto and cross power spectrum data. We will then outline estimates of derived quantities from the model fitting results, such as the redshift distribution of the far and near-IR intensity and the cosmic dust density.

3.4.1 Power spectra

In Figure 3.8, we show the angular auto and cross-power spectra of *Herschel* and *Spitzer* in the Boötes field. The top, middle and bottom panels are for *Herschel* 250, 350 and 500 μm, respectively. The blue solid curve is total best-fit power spectrum for Herschel power spectrum, which is comprised of two components, i.e. FIR galaxies (blue dashed), and total shot-noise (not shown). Similarly, the green solid line is the best-fit for *Spitzer* auto power spectrum, which has contributions given by IHL (green dotted) and NIR faint galaxies (green dashed). As described in Cooray et al. (2012) the shot-noise of *Spitzer* power spectrum can be described by the faint galaxies, though the clustering of such galaxies fall short of the fluctuations power spectrum at tens of arcminute angular scales. The red solid line is the total cross correlation, including a shot-noise term not shown here, while the red dotted and dashed lines separate the cross-correlation to the main terms given by IHL correlating

with faint far-IR dusty galaxies and faint near-IR galaxies correlating with faint far-IR dusty galaxies, respectively. In terms of the cross-correlations we find that these two terms are roughly comparable.

Another comparison of the data and model is shown in Fig. 3.9. Here, we calculate the correlation coefficient separately from the data and compare to the correlation coefficient of the best-fit model. Displaying the information in this way is a valuable check of the relative strength of correlation. As the far-IR wavelength is increased from 250 μm to 500 μm we find a less of a correlation between *Herschel* and *Spitzer*. Not only does the total correlation decrease, from our model fit we also find that the correlation between IHL and dusty far-IR galaxies, as a fraction of the total correlation, is also decreased.

The best-fit values and 1σ errors of the model parameters are shown in Table 3.1. We find the MCMC forces just a shot-noise term, i.e. a straight line, to fit the data if we use data points out to $\ell \sim 10^5$ because the errors at high ℓ (small scales) are very small compared to the errors at large scales. For these reasons, our results are obtained by fitting to the power spectrum data at $\ell < 10^4$, and ignoring all data points at $\ell > 10^4$ in the fitting process.

3.4.2 Intensity redshift distribution

Using the fitting results of the best-fit model parameters and their errors, we estimate the redshift distribution of $d(\nu I_\nu)/dz$ for far-IR dusty galaxies in the three SPIRE bands as

$$\frac{d(\nu I_\nu^{\rm FIR})}{dz} = \frac{c}{H(z)(1+z)^2}\nu\bar{j}_\nu(z), \tag{3.23}$$

where c is the speed of light, $H(z)$ is the Hubble parameter, and $\bar{j}_\nu(z)$ is the mean emissivity given by equation (3.8). Also, the redshift distribution of $d(\nu I_\nu)/dz$ for the IHL component

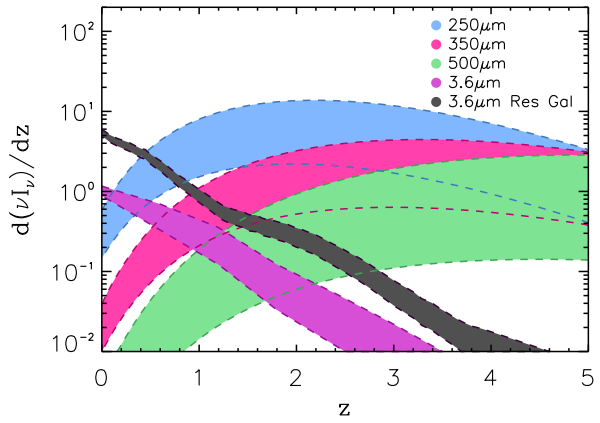

Figure 3.10: Redshift distribution of $d(\nu I_\nu)/dz$ for Herschel FIR galaxies at 250, 350 and 500 μm, and *Spitzer* IHL and residual galaxies at 3.6 μm.

can be obtained by

$$\frac{d(\nu I_\nu^{\rm IHL})}{dz} = \frac{c}{4\pi H(z)(1+z)^2} \int dM n(M,z) \bar{L}_{\rm IHL}, \tag{3.24}$$

where $\bar{L}_{\rm IHL}(M,z)$ is the mean IHL luminosity given by equation (3.14), and $n(M,z)$ is the halo mass function.

In Figure 3.10, we show $d(\nu I_\nu)/dz$ as a function of the redshift for *Herschel* galaxies at 250, 350 and 500 μm, and *Spitzer* IHL and faint unresolved galaxies at 3.6 μm. We find the redshift distribution has a turnover between $z = 1$ and 2 for 250 μm, which indicates the intensity is dominated by the sources at $z = 1 \sim 2$ for 250 μm. For 350 μm, the turnover of $d(\nu I_\nu)/dz$ is not obvious and is shifted to higher redshift around $z = 3$. For 500 μm, we find that the sources at $z > 3$ dominate the intensity. The increase in redshift with the wavelength for dusty sources we find here is consistent with the well-known result in the literature (Bethermin et al., 2011; Amblard et al., 2011; Viero et al., 2013). On the other hand, the $d(\nu I_\nu)/dz$ of *Spitzer* IHL and residual galaxies at 3.6 μm has their maximum values at $z = 0$ and decreases quickly with increasing redshift. This shape, which is substantially different from *Herschel* dusty galaxies, is the main reason that the cross-correlation signal between

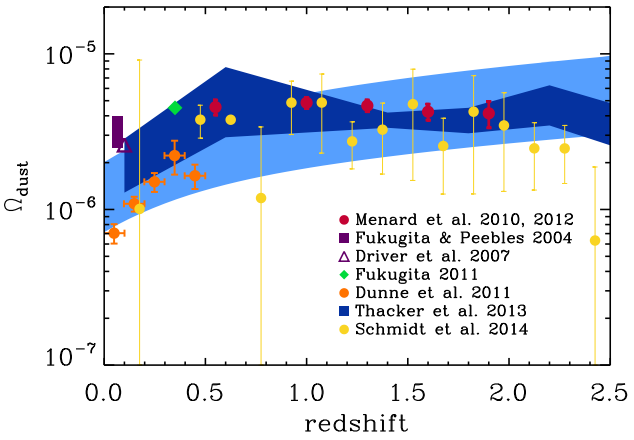

Figure 3.11: The fractional cosmic dust density $\Omega_{\rm dust}$ as a function of redshift from FIR galaxies. The blue shaded region shows the 1σ range of $\Omega_{\rm dust}$ for FIR galaxies derived from our MCMC fitting results. We also show the results from different observations for $\Omega_{\rm dust}$. The orange squares are the measurement of H-ATLAS dust mass function in Dunne et al. (2010), and the other data are based on the extinction measurements of the SDSS and 2dF surveys (Menard et al., 2010; Menard & Fukugita , 2012; Fukugita & Peebles, 2004; Fukugita et al., 2011; Driver et al., 2007). We also include recent measurements from Schmidt et al. (2014) using the cross-correlation between the Planck High Frequency Instrument and quasars from the Sloan Digital Sky Survey DR7. Finally, we include results from Thacker et al. (2013) as the dark blue shaded region.

Herschel and *Spitzer* is below 0.5 at 250 μm with a decrease to a value below 0.2 at 500 μm. The decrease with increasing wavelength is consistent with the overall model description. If naively interpreted, the small cross-correlation with *Herschel* could have been argued as evidence for a very high-redshift origin for the *Spitzer* fluctuations, similar to the arguments that have been for the origin of *Spitzer*-Chandra cross-correlation (Cappelluti et al., 2012). Our modeling suggest the opposite: *Spitzer* fluctuations are very likely to be dominated by a source at $z < 1$ while intensity fluctuations in *Herschel* originate from $z = 1$ and above at 250, 350 and 500 μm.

3.4.3 Cosmic Dust Density

As an application of our models we also derive the fractional cosmic dust density $\Omega_{\rm dust}$ of galaxies from the fitting results. Following Thacker et al. (2013), the $\Omega_{\rm dust}$ for galaxies is given by

$$\Omega_{\rm dust}(z) = \frac{1}{\rho_0} \int dL \Phi(L, z) M_{\rm dust}(L), \tag{3.25}$$

where ρ_0 is the current cosmic critical density, $\Phi(L, z)$ is the luminosity function, and $M_{\rm dust}$ is the dust mass with IR luminosity L with temperature assumed to be $35K$ that we fix in the power spectrum model. We make use of equation (4) of Fu et al. (2012) to estimate $M_{\rm dust}$ from IR luminosity (Thacker et al., 2013). Also, we assume the dust opacity κ_d takes the form as $\kappa_d = A_\kappa \nu^{\beta_d}$, where $\beta_d = 2$ is the dust emissivity spectral index, and A_κ is the normalization factor which is estimated by $\kappa_d = 0.07 \pm 0.02$ m^{2}kg^{-1} at 850 μm (Dunne et al., 2000; James et al., 2002).

We show $\Omega_{\rm dust}$ as a function of redshift in Figure 3.11. The blue shaded region is the 1σ range of the $\Omega_{\rm dust}$ from the FIR. We also show the other measurements for comparison. The orange squares are from the H-ATLAS dust mass function as measured in Dunne et al. (2010), and the other data are based on the extinction measurements of the SDSS and 2dF surveys (Menard et al., 2010; Menard & Fukugita , 2012; Fukugita & Peebles, 2004; Fukugita et al., 2011; Driver et al., 2007). We find our $\Omega_{\rm dust}$ result from galaxies is consistent with the other measurements, which has $\Omega_{\rm dust}$ increasing at higher redshift.

3.5 Summary

We have calculated the cross-correlation power spectrum of the cosmic infrared background at far and near-IR wavelengths using *Herschel* and *Spitzer* in the Boötes field. We measured the correlation coefficient to be between 10-40% with the highest correlation seen in the 250 μm band and the lowest in 500 μm.

Recent results from Cooray et al. (2012) and Zemcov et al. (2014) suggest that the near-IR background anisotropies have mostly a low redshift origin at $z < 1$, arising from intra-halo light and faint dwaft galaxies. Meanwhile the far-IR signal is dominated by dusty galaxies peaking at a redshift of $\sim$1 and above (Amblard et al., 2010; Thacker et al., 2013; Viero et al., 2013). By cross correlating *Herschel* with *Spitzer* we are able to provide a check on the robustness of such a model. We find that not only can such a model fit the auto-correlations they were designed to fit, but can also explain the cross-correlation signal, including the wavelength dependence of the cross-correlation coefficient.

Bibliography

Amblard, A. & Cooray, A. 2007, ApJ, 670, 903

Amblard, A., Cooray, A., Serra, P., et al. 2010, A&A, 518, L9

Amblard, A., et al. 2011, Nature, 470, 510

Arendt, R. G., Fixsen, D. J., & Moseley, S. H. 2000, ApJ, 536, 500

Ashby, M. L. N., et al. 2009, ApJ, 701, 428

Bacon, D., Refregier, A., & Ellis, R. 2000, MNRAS 318, 625

Berta, S., et al. 2011, A&A 532, A49

Bertin, E. & Arnouts, S. 1996, A&AS, 117, 393

Bethermin, M., Dole, H., Lagache, G., et al. 2011, A&A, 529, A4

Bracco, A., Cooray, A. , Veneziani, M. , et al. 2011, MNRAS, 412, 1151

van de Bosch, F.C., Tormen, G., Giocoli, C. 2005, MNR

Cantalupo C. M. , Borrill J. D. , Jaffe, A. H. , et al. 2009 Astrophys. J. Suppl. 187 (2010) 212

Cantalupo, C. M., et al. 2010, ApJS, 187, 212

Cappelluti, N., Kashlinsky, A., and Arendt, R. G., et al. 2012, ApJ, 769, 68

Chapman, J. F. & Wardle, M. 2006 MNRAS, 371, 513

Carollo, D., et al. 2010, ApJ, 712, 692727

Casey, C. M., Berta, S., Bethermin, M., et al. 2012, ApJ accepted

Clements, D.L., Dunne, L., Eales, S. 2010, MNRAS, 403, 274

Cooray, A., Sheth, R.K. 2002, PR, 372, 1

Cooray, A. et al. 2010, A&A, 518, L22

Cooray, A., et al. 2012, Nature, 490, 514

Coppin, K., et al. 2006, MNRAS, 372, 1621

Coppin, K. E. K. , et al. 2011 arXiv:1105.3199 [astro-ph.CO].

Courteau, S., et al. 2011, ApJ, 739, 20

Davies, J. I. , et al. 2012 arxiv:1210.4448 [astro-ph.CO]

De Bernardis, F., & Cooray, A. 2012, ApJ, 760, 14

Dekel, A., Birnboim, Y., Engel, G., et al. 2009, Nature, 457, 451

Dole, H., Lagache, G., Puget, J.-L., et al. 2006, A&A, 451, 417

Dowell, C.D., et al. 2010, Proc. SPIE 7731, 773136

Driver, S. P., et al. 2007, MNRAS, 379, 1022

Dunne, L. , Eales, S. A. , Edmunds, M. G. , et al. 2000, MNRAS, 315, 115

Dunne, L. , Eales, S. , Ivison, R. , et al. 2003, Nature, 424, 285

Dunne, L. , Gomez, H. , da Cunha, E. S., et al. 2010, MNRAS, 417, 1510

Dwek, E., et al. 1998, ApJ, 508, 106

Dye, S., Dunne, L., Eales, S. et al. 2010, A&A, 518, L10

Eales, S., et al. 2010, A&A, 518, L23

Elbaz, D., et al. 2010, A&A, 518, L23

Fixsen, D. J., et al. 1998, ApJ, 508, 123

Fu, H., Jullo, E., Cooray, A., et al. 2012, ApJ, 753, 12

Fukugita, M., Peebles P. J. E., 2004, ApJ, 616, 643

Fukugita, M., 2011, arXiv, arXiv:1103.4191

Galametz, M. et al. 2012, MNRAS, 425, 763

Gelman, A. & Rubin, D. 1992, Statistical Science, 7, 457-472.

Giavalisco, M., & Dickinson, M. 2001, ApJ, 550, 177

Gistpert, R., Lagache, G., & Puget, J.L., 2000, A&A, 360, 1

Glenn, J., et al. 2010, MNRAS, 409, 109

Gonzalez, A. H., Zabludoff, A. I. & Zaritsky, D. 2005, ApJ, 618, 195-213

Gong, Y., & Chen, X. 2007, PRD, 76, 123007

Griffin, M. J. , Abergel, M. J. , Abreu, A. , et al. 2010, A&A, 518, L3

Guo, Q., Cole, S., Lacey, C. et al. 2011, MNRAS, arXiv.org:1011.3048

Helgason, K., Ricotti, M., & Kashlinsky, A. 2012, ApJ, 752, 113

Hickox, R. C. et al. 2012, MNRAS, 421, 284

Hivon, E., et al. 2002, ApJ, 567, 2

Hwang, H.S., Elbaz, D. , Magdis, G. , et al., 2010, MNRAS, 409, 75

James, A. , Dunne, L. et al., 2002 MNRAS, 335, 753

Kampen, E. van, et al. 2012, MNRAS, 426, 3455

Kashlinsky, A., Arendt, R. G., Mather, J., & Moseley, S. H. 2005, Nature, 438, 45

Kashlinsky, A., Arendt, R. G., Mather, J., & Moseley, S. H. 2007, ApJL, 654, L5

Kashlinsky, A., Arendt, R. G., Ashby, M. L. N., Fazio, G. G., Mather, J., & Moseley S. H. 2012, ApJ, 753, 63

Knox, L., et al. 2001, ApJ, 550, 7

Krick, J. E., & Bernstein, R. A. 2007, ApJ, 134, 466-493

Lagache, G., Haner, L. M. , et al. 2000, A&A, 354, 247

Lagache, G., et al. 2007, ApJ, 665, L89

Lapi, A., et al. 2011, ApJ, 742, 1

Lee *et al.*, ApJ 695, 368 (2009)

Levenson, L., Marsden, G., Zemcov, M., et al. 2010, MNRAS, 409, 83

Lewis, A & Bridle, S. 2002, PRD, 66, 103511

Li, A. , Draine, B. T. , 2002, Apj, 572 232

Lin, Y. T., Mohr, J. J., & Stanford, S. A. 2004, ApJ, 610, 745-761

Maddox, S. J., et al. 2010. A&A, 518, L11

Matsumoto, T., Seo, H. J., Jeong, W.-S., Lee, H. M., Matsuura, S., Matsuhara, H., Oyabu, S., Pyo, J., et al. 2011, ApJ, 742, 124

Menard B., Scranton R., Fukugita M., Richards G., 2010, MNRAS, 405, 1025

Menard, B., & Fukugita, M. 2012, ApJ, 754, 116

Metropolis, N., Rosenbluth, A. W., Rosenbluth, M. N., Teller, A. H., & Teller, E. 1953, JCP, 21, 1087

Mitchell-Wynne K. , Cooray A. , Gong Y. et al. 2012, Astrophys. J. 753, 23

Navarro, J. F., Frenk, C. S., White, S. D. M. 1997, ApJ, 490, 493

Negrello M., Hopwood R., De Zotti G., et al. 2010, Science, 330, 800

Nguyen, H. T., Schulz, B., Levenson, L., et al. 2010, A&A, 518, L5

Oliver, S. J., Wang, L., Smith, A. J., Altieri, B., Amblard, A., et al. 2010, A&A, 518, L21

Ott, S. 2010, in Astronomical Society of the Pacific Conference Series, Vol. 434, Astronomical Data Analysis Software and Systems XIX, ed. Y. Mizumoto, K.-I. Morita, & M. Ohishi, 139

Pascale E. , Auld R. , Dariush A. , et al.,arXiv:1010.5782 [astro-ph.IM]

Pei, Y. , 1992, ApJ, 395, 130

Pillbratt, G. L., et al. 2010, A&A, 518, L1

The Planck Collaboration,

Planck Collaboration and Ade, P. A. R., Aghanim, N., Armitage-Caplan, C., Arnaud, M., Ashdown, M., Atrio-Barandela, F., Aumont, J., Baccigalupi, C., Banday, A. J., et al. 2014, A&A,571, A16

Puget, J.L., Abergel, A., Bernard, J.P., et al. 1996, A&A, 308, L5

Purcell, C. W., Bullock, J. S. & Zentner, A. R. 2008, MNRAS, 391, 550-558

T. D. Rawle *et al.* 2010, A&A ,518, L14

Schlegel, D.J. 1998, ApJ, 500, 525

Schmidt, S., Menard, B., et al., 2014, MNRAS 446, 2696

Scott K. S. , Yun M. S. , Wilson G. W. , *et al.*, 2010, MNRAS, 405, 2260. arXiv:1003.1768 [astro-ph.CO]

Shang, C., et al. 2011, arXiv:1109.1522

Sheth, R. K., Tormen, G. 1999, MNRAS, 308, 119

Smidt J. , Amblard A. , Byrnes, C. T. et al. 2010 Phys. Rev. D ,81, 123007

Smith, A. J. , Wang, L. , Oliver, S. J. , et al. arXiv:1109.5186 [astro-ph.CO].

Thacker, C., Cooray, Smidt, et al. 2013, ApJ, 768, 58

Vaccari, M., Marchetti, L., Franceschini, A., et al. 2010, A&A, 518, L20

Valiante, E., Lutz, D., Sturm, E., et al. 2009, ApJ, 701, 1814

Viero, M. P., et al. 2009, ApJ, 707, 1766

Viero, M. P., Wang, L., Zemcov, M., et al. 2013, ApJ, 772, 77

Wardlow, J.L., Cooray, A., et al., 2012, ApJ, submitted arxiv:1205.3778

Xia, J.-Q., et al. 2012, MNRAS, 422, 1324

Yue, B., Ferrara, A., Salvaterra, R., Xu, Y., & Chen, X. 2013, MNRAS, 433, 15561566

Yue, B., Ferrara, A., Salvaterra, R., Xu, Y., & Chen, X. 2014, MNRAS, 440, 1263-1273

Zemcov, M. and Smidt, J. and Arai, T. and Bock, J. and Cooray, A., et al. 2014, Science, 346, 732-735

Appendix A

Appendix

A.1 Cross Power Spectra

Here we discuss the 2-D angular cross-power spectra of Herschel and *Spitzer* in our model. The total cross-power spectrum $C_\ell^{\rm cross}$ is composed of four components which are

$$C_\ell^{\rm cross} = C_\ell^{\rm FIR\times NIR} + C_\ell^{\rm FIR\times IHL}. \tag{A.1}$$

Here $C_\ell = \nu_{\rm obs}\nu'_{\rm obs}C_\ell^{\nu\nu'}$ where $\nu_{\rm obs}$ is the observed frequency at 250, 350 or 500 μm of Herschel survey, and $\nu'_{\rm obs}$ is the observed frequency at 3.6 μm of *Spitzer* survey.

The 1-halo and 2-halo terms of $C_{\ell,\mathrm{FIR}\times\mathrm{NIR}}^{\nu\nu'}$ are given by

$$C_{\ell,\mathrm{FIR}\times\mathrm{NIR}}^{\nu\nu',1\mathrm{h}} = \int dz \left(\frac{d\chi}{dz}\right)\left(\frac{a}{\chi}\right)^2 \bar{j}_\nu(z)\bar{j}_{\nu'}(z) \int dM n(M,z) \frac{\sqrt{\langle N_\mathrm{g}(N_\mathrm{g}-1)\rangle_\nu}\sqrt{\langle N_\mathrm{g}(N_\mathrm{g}-1)\rangle_{\nu'}}}{\bar{n}_\mathrm{g}^\nu(z)\bar{n}_\mathrm{g}^{\nu'}(z)} \sqrt{u^{p_\nu}}\sqrt{u^{p_{\nu'}}}(k|M,z)$$

$$C_{\ell,\mathrm{FIR}\times\mathrm{NIR}}^{\nu\nu',2\mathrm{h}} = \int dz \left(\frac{d\chi}{dz}\right)\left(\frac{a}{\chi}\right)^2 \bar{j}_\nu(z)\bar{j}_{\nu'}(z) \left[\int dM b(M,z) n(M,z) \frac{\langle N_\mathrm{g}\rangle_\nu}{\bar{n}_\mathrm{g}^\nu(z)} u(k|M,z)\right]$$
$$\times \left[\int dM b(M,z) n(M,z) \frac{\langle N_\mathrm{g}\rangle_{\nu'}}{\bar{n}_\mathrm{g}^{\nu'}(z)} u(k|M,z)\right] P_\mathrm{lin}(k,z). \quad (A.3)$$

Here ν and ν' denote FIR and NIR bands for Herschel and *Spitzer* respectively. Then we have $C_{\ell,\mathrm{FIR}\times\mathrm{NIR}}^{\nu\nu'} = C_{\ell,\mathrm{FIR}\times\mathrm{NIR}}^{\nu\nu',1\mathrm{h}} + C_{\ell,\mathrm{FIR}\times\mathrm{NIR}}^{\nu\nu',2\mathrm{h}}$.

The 1-halo and 2-halo terms of $C_{\ell,\mathrm{FIR}\times\mathrm{IHL}}^{\nu\nu'}$ are

$$C_{\ell,\mathrm{FIR}\times\mathrm{IHL}}^{\nu\nu',1\mathrm{h}} = \frac{1}{4\pi}\int dz \left(\frac{d\chi}{dz}\right)\left(\frac{a}{\chi}\right)^2 \bar{j}_\nu(z) \int dM n(M,z) \frac{\sqrt{\langle N_\mathrm{g}(N_\mathrm{g}-1)\rangle_\nu}}{\bar{n}_\mathrm{g}^\nu(z)} \sqrt{u^{p_\nu}(k|M,z)}\bar{L}_\mathrm{IHL}^{\nu'}(M,z)u(k|M,z)$$

$$C_{\ell,\mathrm{FIR}\times\mathrm{IHL}}^{\nu\nu',2\mathrm{h}} = \frac{1}{4\pi}\int dz \left(\frac{d\chi}{dz}\right)\left(\frac{a}{\chi}\right)^2 \bar{j}_\nu(z) \left[\int dM b(M,z) n(M,z) \frac{\langle N_\mathrm{g}\rangle_\nu}{\bar{n}_\mathrm{g}^\nu(z)} u(k|M,z)\right]$$
$$\times \left[\int dM b(M,z) n(M,z) u(k|M,z) \bar{L}_\mathrm{IHL}^{\nu'}(M,z)\right] P_\mathrm{lin}(k,z). \quad (A$$

So we get $C_{\ell,\mathrm{FIR}\times\mathrm{IHL}}^{\nu\nu'} = C_{\ell,\mathrm{FIR}\times\mathrm{IHL}}^{\nu\nu',1\mathrm{h}} + C_{\ell,\mathrm{FIR}\times\mathrm{IHL}}^{\nu\nu',2\mathrm{h}}$.

A.2 Flat Sky Approximation

Using the formalism of Hivon et al. (2002), we show how to get the flat sky approximation which allows the use of Fourier transforms instead of spherical harmonics to calculate the power spectrum. The flat sky approximation requires $\theta \ll 1$ and $\ell \gg 1$. We start by defining

the weighted sum over the multipole moments as

$$M(\vec{\ell}) = \sqrt{\frac{4\pi}{2\ell+1}} \sum_{m=-\ell}^{\ell} i^{-m} M_{\ell m} e^{im\phi_\ell}. \tag{A.6}$$

For this derivation we need the following approximations for when $\theta \ll 1$ and $\ell \gg 1$. The first is known as the Jacobi-Anger expansion of the plane wave,

$$e^{i\vec{\ell}\cdot\vec{r}} = \sum_m i^m J_m(\ell\theta) e^{im(\phi-\phi_\ell)}. \tag{A.7}$$

Where $J_m(\ell\theta)$ are Bessel functions and we use the fact that since θ is small r $\approx \theta$.

Next, to show that $Y_{\ell m}$ is approximately $\sqrt{\ell/2\pi} J_m(\ell m) e^{im\phi}$, we start with the general Legendre equation and perform a change of variables $\cos(\theta) \Rightarrow \cos(\frac{\theta'}{\ell})$. Using the fact that $\theta'/\ell \ll 1$ to simplify, and multiply the equation by θ'^2/ℓ^2 to get it into the correct form. Now, one can recognize the equation as Bessel's equation with solution $J_m(\theta') = J_m(\ell\theta)$

Putting this all together, we decompose the maps into spherical harmonics and introduce our simplifications to get,

$$
\begin{aligned}
M(\hat{n}) &= \sum_{m\ell} M_{\ell m} Y_{\ell m}, \\
&= \sum_{m\ell} M_{\ell m} \sqrt{\frac{\ell}{2\pi}} J_m(\ell m) e^{im\phi}, \\
&= \sum_{m\ell} \frac{\ell}{2\pi} \int \frac{\mathrm{d}\phi_\ell}{2\pi} M(\vec{\ell}) i^m J_m(\ell m) e^{im(\phi-\phi_\ell)}, \\
&\approx \int \frac{\mathrm{d}^2\ell}{(2\pi)^2} M(\vec{\ell}) e^{i\vec{\ell}\cdot\vec{r}}.
\end{aligned}
\tag{A.8}
$$

A.3 Cross Correlation Power Spectrum and Cosmic Variance

Analogous to the convolution theorem, correlations obey a similar relation except with a complex conjugate. Below, $\mathcal{F}$ denotes 2D Fourier transforms and $\star$ denotes cross-correlation, where M_i are 2D maps:

$$
\mathcal{F}(M_1 \star M_2) = \mathcal{F}(M_1) \cdot \mathcal{F}(M_2)^* \,. \tag{A.9}
$$

Since we can use Fourier transforms as a suitable basis to obtain a power spectrum (see A.2 in Appendix), we are guaranteed that the cross-correlation above is also a power spectrum. Putting it together, for a specific ℓ_i bin and including Fourier masking, we obtain

$$
\langle C_{l_i} \rangle = \frac{\sum_{l_1}^{l_2} w(l_x, l_y) \widetilde{M_1}(l_x, l_y) \widetilde{M_2}^*(l_x, l_y)}{\sum_{l_1}^{l_2} w(l_x, l_y)}. \tag{A.10}
$$

Here $\widetilde{M_1} = \mathcal{F}(M_1)$ and $w(l_x, l_y)$ is a Fourier mask that has the value one for modes we

keep and zero for modes we mask. The binning is done in annular rings so $l_1 \geq l_x^2 + l_y^2$ and $l_2 \leq l_x^2 + l_y^2$.

Cosmic variance , δC_ℓ, is the expected variance on the power spectrum estimate at each ℓ mode and is given by

$$\delta C_\ell = \sqrt{\frac{2}{f_{\rm sky}(2\ell+1)\Delta\ell}}(C_\ell^{\rm auto} + N_\ell), \tag{A.11}$$

where N_ℓ is the noise power spectrum generated through jacknife and similar techniques, $f_{\rm sky}$ is the fraction of the sky covered by the map, and $\Delta\ell$ is the width of the ℓ-bin.

For the cross-correation spectrum however, the cosmic variance looks like

$$\delta C_\ell = \sqrt{\frac{1}{f_{\rm sky}(2\ell+1)\Delta\ell}\left[(C_{A\ell}^{\rm auto} + N_{A\ell})(C_{B\ell}^{\rm auto} + N_{B\ell}) + \left(C_\ell^{\rm A\times B}\right)^2\right]}, \tag{A.12}$$

where $C_\ell^{\rm A\times B}$ is the cross-correlation power spectrum.